J. Fluid Mech. (2023), *vol*. 970, A1, doi:10.1017/jfm.2023.503

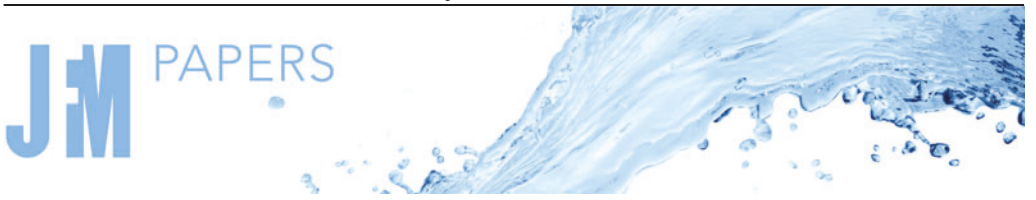

The effect of the spatial variation of the evaporative flux on the deposition from a thin sessile droplet

Hannah-May D'Ambrosio[1], **Stephen K. Wilson**[1],†, **Alexander W. Wray**[1] **and Brian R. Duffy**[1]

[1]Department of Mathematics and Statistics, University of Strathclyde, 26 Richmond Street, Glasgow G1 1XH, UK

(Received 12 September 2022; revised 24 March 2023; accepted 6 June 2023)

A mathematical model for the effect of the spatial variation of the local evaporative flux on the evaporation of and deposition from a thin pinned particle-laden sessile droplet is formulated and solved. We then analyse the behaviour for a one-parameter family of local evaporative fluxes with the free parameter $n\,(>-1)$ that exhibits qualitatively different behaviours mimicking those that can be obtained by, for example, surrounding the droplet with a bath of fluid or using a mask with one or more holes in it to achieve a desired pattern of evaporation enhancement and/or suppression. We show that when $-1 < n < 1$ (including the special cases $n = -1/2$ of diffusion-limited evaporation into an unbounded atmosphere and $n = 0$ of spatially uniform evaporation), all of the particles are eventually advected to the contact line, and so the final deposit is a ring deposit at the contact line, whereas when $n > 1$ all of the particles are eventually advected to the centre of the droplet, and so the final deposit is at the centre of the droplet. In particular, the present work demonstrates that a singular (or even a non-zero) evaporative flux at the contact line is not an essential requirement for the formation of a ring deposit. In addition, we calculate the paths of the particles when diffusion is slower than both axial and radial advection, and show that in this regime all of the particles are captured by the descending free surface before eventually being deposited onto the substrate.

Key words: drops, particle/fluid flow, coupled diffusion and flow

† Email address for correspondence: s.k.wilson@strath.ac.uk

1. Introduction

The evaporation of sessile droplets plays a key role in a wide variety of practical contexts, including agricultural spraying (Tredenick *et al.* 2021), the preparation of chemical and biological assays (Garcia-Cordero & Fan 2017) and inkjet printing (Kuang, Wang & Song 2014). As a consequence, there have been extensive experimental, numerical and theoretical investigations of this problem in recent years (see for example the books and review articles by Cazabat & Guéna 2010; Erbil 2012; Routh 2013; Kovalchuk, Trybala & Starov 2014; Brutin 2015; Lohse & Zhang 2015; Zhong, Crivoi & Duan 2015; Talbot *et al.* 2016; Brutin & Starov 2018; Giorgiutti-Dauphiné & Pauchard 2018; Zang *et al.* 2019; Brutin & Sefiane 2022; Gelderblom, Diddens & Marin 2022; Wilson & D'Ambrosio 2023 and the many references therein).

In practice, droplets often contain non-volatile solutes and/or small particles in suspension (hereafter, referred to simply as 'particles'). In many industrial and scientific processes, the primary concern is the spatial distribution of the final deposit of particles left behind on the substrate after a particle-laden droplet has completely evaporated. In some applications, such as, for example, in DNA chip manufacturing (Dugas, Broutin & Souteyrand 2005) and inkjet printing (Park & Moon 2006), the desired outcome is a uniform final deposit. However, in other applications different final deposit shapes are required, such as, for example, rings in disease diagnostics (Trantum, Wright & Haselton 2012) and for conductive coatings (Layani *et al.* 2009), multiple or concentric rings in the production of resonators in optical communications (Hong, Xu & Lin 2006), and small concentrated deposits in mass spectrometry (Kudina, Eral & Mugele 2016). As a consequence of both the number of practical applications and the wide variety of possible final deposit shapes, the deposition from an evaporating droplet has been the subject of extensive investigation in recent years (see for example the review articles by Kuang *et al.* 2014; Larson 2014; Sefiane 2014; Anyfantakis & Baigl 2015; Zhong *et al.* 2015; Giorgiutti-Dauphiné & Pauchard 2018; Mampallil & Eral 2018; Parsa, Harmand & Sefiane 2018; Al-Milaji & Zhao 2019; Zang *et al.* 2019; Kolegov & Barash 2020; Shao *et al.* 2020; Yang *et al.* 2021; Thampi & Basavaraj 2023), much of it building upon the pioneering work of Deegan *et al.* (1997, 2000) and Deegan (2000).

Particular attention has been paid to the so-called 'coffee-stain' effect (also called the 'coffee-ring' or 'ring-stain' effect) described by Deegan *et al.* (1997, 2000), in which a ring-shaped deposit (i.e. the 'coffee stain') is formed near the contact line of a pinned droplet (i.e. a droplet whose contact line does not move) as it evaporates. For a droplet with strong surface-tension effects, the adjustment of the free surface of the droplet is quasi-steady, and when the evaporation is diffusion limited (see for example Picknett & Bexon 1977) it induces a flow within a thin pinned droplet that carries the particles towards its contact line (see for example Gelderblom *et al.* 2022). The solutions for the flow within a thin pinned droplet were given by Hu & Larson (2005) and Boulogne, Ingremeau & Stone (2017) for diffusion-limited evaporation and by Boulogne *et al.* (2017) for spatially uniform evaporation. The solutions for the flow within a non-thin droplet with either a pinned or an unpinned contact line evaporating according to a modified version of the diffusion-limited model were given by Masoud & Felske (2009). Further details regarding the flow within an evaporating droplet with either a pinned or an unpinned contact line are given in the recent review article by Gelderblom *et al.* (2022). Under the assumption that the suspension of particles is sufficiently dilute that the presence of the particles does not affect the flow, expressions for the mass of particles in a ring deposit from a thin pinned droplet were given by Deegan *et al.* (2000) and Boulogne *et al.* (2017) for diffusion-limited evaporation and by Boulogne *et al.* (2017) for spatially uniform evaporation.

Boulogne *et al.* (2017) compared their theoretical predictions for the growth of a ring deposit with experimental observations for both diffusion-limited and spatially uniform evaporation, and found good agreement between theory and experiment in both situations. Many other experimental studies have been conducted to investigate the formation of a ring deposit, including those by Deegan *et al.* (1997, 2000), Deegan (2000), Kajiya, Kaneko & Doi (2008), Bodiguel & Leng (2010), Marín *et al.* (2011*a*,*b*), Berteloot *et al.* (2012) and Askounis *et al.* (2013). In particular, Marín *et al.* (2011*a*,*b*) observed that the well-known 'rush-hour effect', i.e. the rapid acceleration of the flow towards the contact line during the final stages of evaporation, previously discussed by Deegan *et al.* (2000) and also reported by Hamamoto, Christy & Sefiane (2011), results in a lack of order of the particles near the inner boundary of a ring deposit.

Various authors have extended the analysis of Deegan *et al.* (1997, 2000) to more complicated situations. For example, Popov (2005) and Zheng (2009) modelled the shape of a ring deposit, Tarasevich, Vodolazskaya & Isakova (2011), Vodolazskaya & Tarasevich (2011) and Kaplan & Mahadevan (2015) considered various situations in which the presence of the particles affects the flow within the droplet, Crivoi & Duan (2013) and Crivoi, Zhong & Duan (2015) investigated the effect of particle aggregation on the shape of the final deposit, Sáenz *et al.* (2017) and Wray & Moore (2023) studied non-axisymmetric contact-line deposits arising from non-axisymmetric droplets, and Wray, Duffy & Wilson (2020) and Wray *et al.* (2021) analysed non-axisymmetric contact-line deposits arising from multiple interacting droplets. In addition, Moore, Vella & Oliver (2021) analysed the effects of particle diffusion in a boundary layer near the contact line in which the concentration of particles becomes large and, in particular, investigated the limitations of the assumption that the suspension of particles is dilute.

Since the primary concern in many industrial and scientific processes is the spatial distribution of the final deposit, a variety of ways to control the shape of the final deposit have been explored in the literature (see for example the review articles by Kuang *et al.* 2014; Larson 2014; Sefiane 2014; Anyfantakis & Baigl 2015; Zhong *et al.* 2015; Mampallil & Eral 2018; Parsa *et al.* 2018; Al-Milaji & Zhao 2019; Kolegov & Barash 2020; Shao *et al.* 2020; Yang *et al.* 2021). Control over deposition can be achieved by influencing the flow within the droplet through, for example, contact-line de-pinning (see for example Man & Doi 2016; Patil *et al.* 2016; Li *et al.* 2020), the presence of Marangoni flow (see for example Hu & Larson 2006; Ristenpart *et al.* 2007; Parsa *et al.* 2015; Malinowski *et al.* 2018) or by imposing an electric field (see for example Eral *et al.* 2011; Wray *et al.* 2014), as well as by promoting particle trapping or gelation through, for example, particle–free-surface, particle–particle and particle–substrate interactions (see for example Bhardwaj *et al.* 2010; Yunker *et al.* 2011; Anyfantakis *et al.* 2015; Crivoi *et al.* 2015; Anyfantakis, Baigl & Binks 2017; Kim *et al.* 2016; Zigelman & Manor 2018*a*,*b*).

Another method commonly used to alter the flow within an evaporating droplet, and hence to control the shape of the final deposit, is to alter the environment surrounding the droplet, and hence the local and total evaporative fluxes from it. In particular, several authors have performed experimental studies in which they were able to change the shape of the final deposit by surrounding the droplet with a bath of fluid such that the level of the bath coincided with the base of the droplet and/or confining the droplet within a chamber to suppress evaporation near the contact line (see for example Deegan *et al.* 2000; Kajiya *et al.* 2008), 'masking', i.e. placing the droplet underneath a mask with holes in it in order to achieve a desired pattern of evaporation enhancement and/or suppression (see for example Harris *et al.* 2007; Harris & Lewis 2008; Harris, Conrad & Lewis 2009), increasing the relative humidity of the atmosphere to decrease the evaporation

from the droplet (see for example Chhasatia, Joshi & Sun 2010; Bou Zeid & Brutin 2013), reducing the ambient pressure to increase the evaporation from the droplet (see for example Askounis *et al.* 2014), and using an imposed airflow in the atmosphere to enhance the evaporation from the centre of the droplet (see for example Yang *et al.* 2021).

The concept of masking as a simple way of controlling the deposition process was first explored by Routh & Russel (1998) for evaporating thin films, and subsequently by Deegan *et al.* (2000) for evaporating droplets. In particular, Deegan *et al.* (2000) carried out pioneering experiments involving a droplet evaporating under different ambient conditions. They found that when a pinned droplet evaporates into an effectively unbounded atmosphere and when it is surrounded by a bath of fluid, corresponding to diffusion-limited and approximately spatially uniform evaporation, respectively, a ring deposit forms near the contact line. However, rather more unexpectedly, they also found that when a droplet is confined within a chamber with a hole at its centre, resulting in a local evaporative flux that is approximately proportional to the rate of decrease of the height of the droplet, the evaporation 'produced little redistribution of the solute'. Motivated by this work, Fischer (2002) numerically investigated the effect of three qualitatively different local evaporative fluxes on the final deposit. In particular, they found that while evaporation that was either strongest near the contact line or approximately spatially uniform produced a ring deposit near the contact line, evaporation that was strongest at the centre of the droplet produced a deposit near the centre of the droplet. Subsequently, Harris *et al.* (2007) investigated the effect of manipulating the spatial variation of the local evaporative flux by evaporating droplets under a mask with multiple holes. The mask induced periodic variations in the local evaporative flux and produced final deposits that were concentrated below the holes in the mask, i.e. the mask provided a template for the shape of the final deposit. Tarasevich, Vodolazskaya & Sakharova (2016) developed a theoretical model using an idealised local evaporative flux to mimic the influence of a mask with three or four circular holes above the droplet in order to simulate the behaviour observed experimentally by Harris *et al.* (2007). Vodolazskaya & Tarasevich (2017) generalised this model to account for the diffusion of vapour in the atmosphere, used this model to calculate the local evaporative flux numerically, and investigated the effects of the distance between the mask and the droplet, the radius of the holes in the mask and the spacing between the holes, on both the local evaporative flux and the shape of the final deposit. One restriction on the practical use of masking is that it typically reduces the overall evaporation rate from the droplets and therefore typically lengthens the total drying time (see for example Kajiya *et al.* 2008; Georgiadis *et al.* 2013).

Motivated by the continuing interest in controlling the deposition from an evaporating droplet, in the present work we analyse the effect of the spatial variation of the local evaporative flux on the deposition from a pinned particle-laden sessile droplet. Specifically, in §§ 2–6 we formulate and solve a mathematical model for the evolution of a thin sessile droplet with a general prescribed steady local evaporative flux, the flow within the droplet, the concentration of particles within the droplet, and the masses of the particles in the bulk of the droplet and in the ring deposit that can form at the contact line. Then in §§ 7 and 8 we analyse the behaviour of the general solutions obtained in §§ 3–6 for a particular one-parameter family of local evaporative fluxes. Finally, in § 9 we summarise our main conclusions and indicate some promising directions for future work.

2. Problem formulation

Consider the evaporation of a thin axisymmetric sessile droplet on a planar substrate with a pinned circular contact line with constant radius $\hat{R}_0$. We assume that the suspension

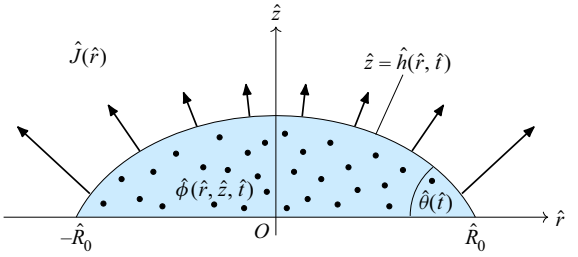

Figure 1. Sketch of a thin pinned particle-laden sessile evaporating droplet on a planar substrate. The droplet has constant contact radius $\hat{R}_0$, contact angle $\hat{\theta}(\hat{t})$, free surface $\hat{z} = \hat{h}(\hat{r}, \hat{t})$ and concentration of particles within the droplet $\hat{\phi}(\hat{r}, \hat{z}, \hat{t})$. The arrows indicate the local evaporative mass flux $\hat{J}(\hat{r})$.

of particles is sufficiently dilute that the presence of the particles does not affect the flow, and refer the description to cylindrical polar coordinates $(\hat{r}, \varphi, \hat{z})$ with $O\hat{z}$ along the axis of symmetry of the droplet, perpendicular to the substrate at $\hat{z} = 0$, as sketched in figure 1. The contact angle, free surface and volume of the droplet are denoted by $\hat{\theta} = \hat{\theta}(\hat{t})$, $\hat{h} = \hat{h}(\hat{r}, \hat{t})$ and $\hat{V} = \hat{V}(\hat{t})$, respectively, where $\hat{t}$ denotes time. The initial values of $\hat{\theta}$ and $\hat{V}$ at $\hat{t} = 0$ are denoted by $\hat{\theta}_0$ and $\hat{V}_0$, respectively. The droplet is deposited onto the substrate at $\hat{t} = 0$, and thereafter its volume decreases until it has completely evaporated, i.e. until $\hat{V}(\hat{t}_{lifetime}) = 0$, where $\hat{t}_{lifetime}$ denotes the lifetime of the droplet.

The velocity and pressure within the droplet, denoted by $\hat{\boldsymbol{u}} = (\hat{u}(\hat{r}, \hat{z}, \hat{t}), 0, \hat{w}(\hat{r}, \hat{z}, \hat{t}))$ and $\hat{p} = \hat{p}(\hat{r}, \hat{z}, \hat{t})$, satisfy the usual mass-conservation and Stokes equations subject to no-slip and no-penetration conditions on the substrate and stress and kinematic conditions on the free surface of the droplet. The concentration of particles within the droplet, denoted by $\hat{\phi} = \hat{\phi}(\hat{r}, \hat{z}, \hat{t})$, satisfies an advection–diffusion equation subject to no-flux conditions on both the substrate and the free surface of the droplet.

The form of the local evaporative mass flux from the free surface of the droplet, denoted by $\hat{J} = \hat{J}(\hat{r}, \hat{t})$ $(\geqslant 0)$, depends on the physical mechanism(s) controlling the evaporation (see for example Wilson & D'Ambrosio 2023). In §§ 3–6 we assume that the local evaporative flux is steady and takes the general form $\hat{J} = \hat{J}(\hat{r})$, where $\hat{J}$ is a prescribed function of $\hat{r}$. Then in §§ 7 and 8 we consider a particular one-parameter family of local evaporative fluxes. In Appendix A we show how the analysis in §§ 3–6 can be generalised to the situation in which the local evaporative flux is unsteady and takes the general separable form $\hat{J} = \hat{J}(\hat{r}, \hat{t}) = \hat{f}(\hat{r})\hat{g}(\hat{t})$, where $\hat{f}$ and $\hat{g}$ are prescribed functions of $\hat{r}$ and $\hat{t}$, respectively, as investigated numerically by Fischer (2002).

Before proceeding further, we non-dimensionalise and scale the variables appropriately for a thin droplet (i.e. in the limit of small contact angle) according to

$$\left.\begin{gathered} \hat{r} = \hat{R}_0 r, \quad \hat{z} = \hat{\theta}_0 \hat{R}_0 z, \quad \hat{\theta} = \hat{\theta}_0 \theta, \quad \hat{h} = \hat{\theta}_0 \hat{R}_0 h, \quad \hat{V} = \hat{\theta}_0 \hat{R}_0^3 V, \quad \hat{t} = \frac{\hat{R}_0}{\hat{U}_{ref}} t, \\ \hat{u} = \hat{U}_{ref} u, \quad \hat{w} = \hat{\theta}_0 \hat{U}_{ref} w, \quad \hat{p} - \hat{p}_a = \frac{\hat{\gamma}\hat{\theta}_0}{\hat{R}_0} p, \quad \hat{\phi} = \hat{\phi}_{ref} \phi, \quad \hat{J} = \hat{J}_{ref} J, \end{gathered}\right\} \tag{2.1}$$

where $\hat{\gamma}$ is the constant surface tension of the fluid, $\hat{p}_a$ is the constant atmospheric pressure, $\hat{U}_{ref} = \hat{J}_{ref}/(\hat{\rho}\hat{\theta}_0)$ is an appropriate characteristic radial velocity scale, in which $\hat{\rho}$ is the constant density of the fluid, $\hat{J}_{ref}$ is an appropriate characteristic local evaporative flux

scale which depends on the physical mechanism(s) controlling evaporation and $\hat{\phi}_{ref}$ is an appropriate characteristic particle concentration scale, chosen to be the spatial average of the initial concentration of particles.

In the present work we are primarily (but not exclusively) motivated by situations in which evaporation is described by the basic quasi-steady diffusion-limited model for the concentration of vapour in the atmosphere (see for example Picknett & Bexon 1977; Popov 2005; Barash *et al.* 2009; Wilson & Duffy 2022; Wilson & D'Ambrosio 2023), subject to a variety of different boundary conditions corresponding to, for example, surrounding the droplet with a bath of fluid or using a mask with one or more holes in it to achieve a desired pattern of evaporation enhancement and/or suppression. In particular, for the diffusion-limited evaporation of a thin droplet appropriate characteristic radial velocity and local evaporative flux scales are

$$\hat{U}_{ref} = \frac{\hat{D}(\hat{c}_{sat} - \hat{c}_{\infty})}{\hat{\rho}\hat{\theta}_0\hat{R}_0}, \quad \hat{J}_{ref} = \frac{\hat{D}(\hat{c}_{sat} - \hat{c}_{\infty})}{\hat{R}_0}, \tag{2.2a,b}$$

where $\hat{D}$ is the constant diffusion coefficient of vapour in the atmosphere, $\hat{c}_{sat}$ is the constant saturation concentration of vapour in the atmosphere and $\hat{c}_{\infty}$ is the constant ambient concentration of vapour in the atmosphere (see for example Wilson & Duffy 2022). For the simplest and most widely studied case of a thin droplet evaporating into an unbounded atmosphere the local evaporative flux is given by the well-known expression

$$J = \frac{2}{\pi}(1 - r^2)^{-1/2}. \tag{2.3}$$

Note that the basic diffusion-limited model has been extended to include a variety of additional physical effects (such as, for example, the dependence of $\hat{c}_{sat}$ on temperature and buoyancy-driven convection in the atmosphere) and/or to relax the assumption of quasi-steadiness, but in the present work we restrict our attention to the basic model. However, even for the basic diffusion-limited model, depending on the specific boundary conditions imposed, it may be either difficult or impossible to obtain a closed-form solution for the concentration of vapour in the atmosphere, and hence to determine a closed-form expression for the local evaporative flux. Thus, as previously mentioned, in the present work we follow an alternative (and more pragmatic) approach similar in spirit to that taken by Fischer (2002) and analyse a one-parameter family of local evaporative fluxes which includes members with the same qualitative features as those found experimentally and/or hypothesised theoretically by previous authors. However, it should be noted that the results obtained in the present work do not rely on this specific motivation for the form of the local evaporative flux.

3. The evolution of the droplet

We consider the situation in which the droplet is sufficiently small that the effect of gravity is negligible, and the surface tension is sufficiently strong that the profile of the droplet evolves quasi-statically. More specifically, we consider the situation in which the appropriately defined Bond number Bo and capillary number Ca, namely

$$Bo = \frac{\hat{\rho}\hat{g}\hat{R}_0^2}{\hat{\gamma}} \quad \text{and} \quad Ca = \frac{\hat{\mu}\hat{U}_{ref}}{\hat{\theta}_0^3\hat{\gamma}}, \tag{3.1a,b}$$

respectively, where $\hat{g}$ is the magnitude of acceleration due to gravity and $\hat{\mu}$ is the constant dynamic viscosity of the fluid, are both small and satisfy $\hat{\theta}_0^2, Bo \ll Ca \ll 1$.

We seek an asymptotic solution for the pressure p in the form

$$p = p^{(0)} + Ca\,p^{(1)} + O(\hat{\theta}_0^2, Bo, Ca^2). \tag{3.2}$$

Note that the pressure p and concentration of particles ϕ are the only quantities that we require beyond leading order, and so, for clarity, we omit the '(0)' superscript on all other leading-order quantities.

At leading order, the Stokes equation yields $\partial p^{(0)}/\partial r = \partial p^{(0)}/\partial z = 0$, and hence the leading-order pressure is independent of r and z, i.e. $p^{(0)} = p^{(0)}(t)$, and is given by the normal stress condition at the free surface to be

$$p^{(0)} = -\frac{1}{r}\frac{\partial}{\partial r}\left(r\frac{\partial h}{\partial r}\right). \tag{3.3}$$

The free-surface profile of the droplet $h(r, t)$ therefore satisfies

$$\frac{\partial}{\partial r}\left(\frac{1}{r}\frac{\partial}{\partial r}\left(r\frac{\partial h}{\partial r}\right)\right) = 0, \tag{3.4}$$

subject to $h = 0$ and $\partial h/\partial r = -\theta$ at $r = 1$ together with the requirement that $h(0, t)$ must be finite, and hence takes the familiar paraboloidal form

$$h = \frac{\theta(1 - r^2)}{2}. \tag{3.5}$$

Evaluating (3.3) using (3.5) yields $p^{(0)} = 2\theta$. For the purpose of the present work, it is convenient to express h as

$$h = \theta\eta, \quad \text{where } \eta(r) = \frac{1 - r^2}{2}. \tag{3.6}$$

The volume $V = V(t)$ of the droplet is given by

$$V = 2\pi \int_0^1 h(r, t) r\,\mathrm{d}r = 2\pi\theta H(1) = \frac{\pi\theta}{4}, \tag{3.7}$$

where $H = H(r)$, defined by

$$H = \int_0^r \eta(\tilde{r})\,\tilde{r}\,\mathrm{d}\tilde{r} = \frac{1 - (1 - r^2)^2}{8}, \tag{3.8}$$

is the incomplete radial integral of ηr. For future reference we note that $H(1) = 1/8$.

The droplet evolves according to the global mass-conservation condition

$$\frac{\mathrm{d}V}{\mathrm{d}t} = -F, \tag{3.9}$$

where F, defined by

$$F = 2\pi \int_0^1 J(\tilde{r})\,\tilde{r}\,\mathrm{d}\tilde{r} = 2\pi I(1), \tag{3.10}$$

is the (constant) total evaporative mass flux from the free surface of the droplet, in which $I = I(r)$, defined by

$$I = \int_0^r J(\tilde{r})\,\tilde{r}\,\mathrm{d}\tilde{r}, \tag{3.11}$$

is the incomplete radial integral of $J r$. The initial values of θ and V are given by $\theta = \theta_0 = 1$ and $V = V_0 = \pi/4$. Substituting the expression for V given by (3.7) into (3.9)

with (3.10) yields

$$\frac{\mathrm{d}V}{\mathrm{d}t} = 2\pi\frac{\mathrm{d}\theta}{\mathrm{d}t}H(1) = -2\pi I(1), \tag{3.12}$$

and solving (3.12) shows that the droplet evolves according to

$$\theta = 1 - \frac{I(1)}{H(1)}t, \quad V = \frac{\pi}{4}\left(1 - \frac{I(1)}{H(1)}t\right). \tag{3.13a,b}$$

Setting $V = 0$ in (3.13*a*,*b*) shows that the lifetime of the droplet is given by

$$t_{lifetime} = \frac{H(1)}{I(1)}. \tag{3.14}$$

Note that in the special case of diffusion-limited evaporation into an unbounded atmosphere for which J is given by (2.3), (3.11) yields $I(1) = 2/\pi$, (3.10) gives $F = 2\pi I(1) = 4$ and (3.14) recovers the familiar expression for the lifetime of a thin pinned droplet, namely $t_{lifetime} = \pi/16$ (see for example Stauber *et al.* 2014; Wilson & Duffy 2022).

4. The flow within the droplet

At leading order the mass-conservation equation is

$$\frac{1}{r}\frac{\partial(ru)}{\partial r} + \frac{\partial w}{\partial z} = 0, \tag{4.1}$$

and at first order the Stokes equation reduces to

$$\frac{\partial^2 u}{\partial z^2} = \frac{\partial p^{(1)}}{\partial r}, \quad 0 = \frac{\partial p^{(1)}}{\partial z} \tag{4.2a,b}$$

(see for example Wray *et al.* 2021). In particular, (4.2*b*) shows that the first-order pressure $p^{(1)}$ is independent of z, i.e. $p^{(1)} = p^{(1)}(r, t)$. Solving (4.1) and (4.2) subject to the no-slip and no-penetration conditions on the substrate, i.e. $u(r, 0, t) = w(r, 0, t) = 0$, and the tangential stress condition on the free surface of the droplet,

$$\frac{\partial u}{\partial z} = 0 \quad \text{on } z = h, \tag{4.3}$$

leads to

$$u = \frac{1}{2}\frac{\partial p^{(1)}}{\partial r}\left(z^2 - 2hz\right) \tag{4.4}$$

and

$$w = \frac{z^2}{6r}\left[\frac{\partial p^{(1)}}{\partial r}\left(3r\frac{\partial h}{\partial r} + 3h - z\right) + \frac{\partial^2 p^{(1)}}{\partial r^2}r\,(3h - z)\right]. \tag{4.5}$$

The kinematic condition can be expressed as

$$\frac{\partial h}{\partial t} + \frac{1}{r}\frac{\partial(rQ)}{\partial r} = -J, \tag{4.6}$$

where $Q = Q(r, t)$, defined by

$$Q = \int_0^h u \, \mathrm{d}z = h\bar{u}, \tag{4.7}$$

is the local radial volume flux of fluid, and $\bar{u} = \bar{u}(r, t)$, defined by

$$\bar{u} = \frac{1}{h}\int_0^h u \, \mathrm{d}z, \tag{4.8}$$

is the depth-averaged radial velocity. Substituting the expression for u given by (4.4) into (4.7) yields

$$Q = -\frac{h^3}{3}\frac{\partial p^{(1)}}{\partial r}. \tag{4.9}$$

For the purpose of the present work, it is convenient to express Q in terms of the incomplete integrals H and I given by (3.8) and (3.11), respectively, by integrating (4.6) with respect to r and rearranging to give

$$Q = -\frac{1}{r}\int_0^r \left(J + \frac{\partial h}{\partial t}\right)\tilde{r}\,\mathrm{d}\tilde{r} = -\frac{1}{r}\left(\int_0^r J(\tilde{r})\,\tilde{r}\,\mathrm{d}\tilde{r} + \frac{\mathrm{d}\theta}{\mathrm{d}t}\int_0^r \eta(\tilde{r})\,\tilde{r}\,\mathrm{d}\tilde{r}\right), \tag{4.10}$$

and hence obtaining the explicit expression

$$Q = \frac{I(1)H(r) - H(1)I(r)}{rH(1)}. \tag{4.11}$$

In particular, (4.11) shows that Q (but not, of course, $\bar{u}$) is independent of time t. Eliminating Q between (4.9) and (4.11) and recalling that h is given by (3.5) gives

$$\frac{\partial p^{(1)}}{\partial r} = -\frac{24\,[I(1)H(r) - H(1)I(r)]}{\theta^3 r(1-r^2)^3 H(1)}, \tag{4.12}$$

and explicit expressions for the velocities u and w are given by substituting (4.12) into (4.4) and (4.5).

5. The concentration of particles within the droplet

The concentration of particles within the droplet ϕ satisfies the advection–diffusion equation

$$Pe^*\left(\frac{\partial \phi}{\partial t} + u\frac{\partial \phi}{\partial r} + w\frac{\partial \phi}{\partial z}\right) = \hat{\theta}_0^2\frac{1}{r}\frac{\partial}{\partial r}\left(r\frac{\partial \phi}{\partial r}\right) + \frac{\partial^2 \phi}{\partial z^2}, \tag{5.1}$$

in which Pe^* is the appropriately defined reduced Péclet number which characterises the ratio of advective and diffusive particle transport timescales, namely

$$Pe^* = \frac{\hat{\theta}_0^2 \hat{R}_0 \hat{U}_{ref}}{\hat{D}_p}, \tag{5.2}$$

where $\hat{D}_p$ is the constant diffusivity of the particles in the fluid. Equation (5.1) is subject to the no-flux conditions

$$\frac{\partial \phi}{\partial z} = 0 \quad \text{on } z = 0 \tag{5.3}$$

and

$$\frac{1}{\sqrt{1+\hat{\theta}_0^2\,(\partial h/\partial r)^2}}\left(\frac{\partial \phi}{\partial z}-\hat{\theta}_0^2\frac{\partial h}{\partial r}\frac{\partial \phi}{\partial r}\right)=Pe^*J\phi \quad \text{on } z=h. \tag{5.4}$$

In most of the remainder of the present work we consider the regime in which diffusion is faster than axial advection but slower than radial advection, i.e. we consider the regime in which the reduced Péclet number satisfies $\hat{\theta}_0^2 \ll Pe^* \ll 1$, and seek an asymptotic solution for ϕ in the form

$$\phi=\phi^{(0)}+Pe^*\phi^{(1)}+O\left(\hat{\theta}_0^2, Pe^{*2}\right). \tag{5.5}$$

However, note that in § 8 we calculate the paths of the particles in the alternative regime in which diffusion is slower than both axial and radial advection, i.e. when the reduced Péclet number satisfies $Pe^* \gg 1$.

At leading order, (5.1), (5.3) and (5.4) reduce to

$$\frac{\partial^2\phi^{(0)}}{\partial z^2}=0, \tag{5.6}$$

subject to

$$\frac{\partial\phi^{(0)}}{\partial z}=0 \quad \text{on } z=0 \text{ and } z=h, \tag{5.7}$$

which shows that $\phi^{(0)}$ is independent of z, i.e. $\phi^{(0)}=\phi^{(0)}(r,t)$.

At first order, (5.1), (5.3) and (5.4) reduce to

$$\frac{\partial^2\phi^{(1)}}{\partial z^2}=\frac{\partial\phi^{(0)}}{\partial t}+u\frac{\partial\phi^{(0)}}{\partial r}, \tag{5.8}$$

subject to

$$\frac{\partial\phi^{(1)}}{\partial z}=0 \quad \text{on } z=0 \tag{5.9}$$

and

$$\frac{\partial\phi^{(1)}}{\partial z}=J\phi^{(0)} \quad \text{on } z=h. \tag{5.10}$$

Integrating (5.8) with respect to z subject to (5.9) and (5.10), and henceforth dropping the superscript '(0)' on ϕ for clarity, yields the equation for the leading-order concentration of particles, namely

$$\frac{\partial\phi}{\partial t}+\bar{u}\frac{\partial\phi}{\partial r}=\frac{J\phi}{h}, \tag{5.11}$$

where the depth-averaged radial velocity $\bar{u}$ is given by (4.8) (see for example Deegan *et al.* 2000; Wray *et al.* 2014, 2021).

Equation (5.11) may be put into characteristic form, i.e.

$$\frac{\mathrm{d}\phi}{\mathrm{d}t}=\frac{J\phi}{h} \quad \text{on the characteristics determined by} \quad \frac{\mathrm{d}r}{\mathrm{d}t}=\bar{u}, \tag{5.12}$$

subject to a prescribed initial concentration of particles in the bulk of the droplet, $\phi(r,0)=\phi_0(r)$, and solved using the method of characteristics. Using the expressions for h and

$\mathrm{d}\theta/\mathrm{d}t$ given by (3.6) and (3.12), the characteristic equations (5.12) can be used to write

$$\frac{\mathrm{d}r}{\mathrm{d}\theta} = \frac{\mathrm{d}r/\mathrm{d}t}{\mathrm{d}\theta/\mathrm{d}t} = -\frac{H(1)Q(r)}{\theta I(1)\eta(r)}, \quad \frac{\mathrm{d}\phi}{\mathrm{d}r} = \frac{\mathrm{d}\phi/\mathrm{d}t}{\mathrm{d}r/\mathrm{d}t} = \frac{J(r)\phi}{Q(r)}. \tag{5.13a,b}$$

Integration of (5.13*a*,*b*) yields the implicit solution

$$\log\theta = -\int_{r_0}^{r} \frac{I(1)\eta(\tilde{r})}{H(1)Q(\tilde{r})}\,\mathrm{d}\tilde{r}, \quad \log\frac{\phi}{\phi_0} = \int_{r_0}^{r} \frac{J(\tilde{r})}{Q(\tilde{r})}\,\mathrm{d}\tilde{r}, \tag{5.14a,b}$$

where $r_0 = r_0(r,t)$ $(0 \leqslant r_0 \leqslant 1)$ denotes the initial radial position (i.e. the radial position at time $t = 0$) of the particles that are at radial position r at time t (see for example Boulogne *et al.* 2017), and is determined by solving (5.14*a*). Note that, by definition, $r_0(r,0) = r$. The solution (5.14) can be simplified by adding (5.14*a*) and (5.14*b*) to yield

$$\log\theta + \log\frac{\phi}{\phi_0} = -\int_{r_0}^{r} \frac{I(1)\eta(\tilde{r}) - H(1)J(\tilde{r})}{H(1)Q(\tilde{r})}\,\mathrm{d}\tilde{r}, \tag{5.15}$$

and then recalling that Q may be expressed in the form (4.11) to give

$$\log\theta + \log\frac{\phi}{\phi_0} = -\int_{r_0}^{r} \frac{1}{\tilde{r}Q(\tilde{r})}\frac{\mathrm{d}\,(\tilde{r}Q(\tilde{r}))}{\mathrm{d}\tilde{r}}\,\mathrm{d}\tilde{r} = \log\frac{r_0Q(r_0)}{rQ(r)}. \tag{5.16}$$

Hence the implicit solution (5.14) of the characteristic equations (5.12) may be written in the simplified form

$$\log\theta = -\int_{r_0}^{r} \frac{I(1)\eta(\tilde{r})}{H(1)Q(\tilde{r})}\,\mathrm{d}\tilde{r}, \quad \frac{\phi}{\phi_0} = \frac{r_0Q(r_0)}{\theta rQ(r)}. \tag{5.17a,b}$$

As mentioned in § 2, the corresponding analysis for the situation in which the local evaporative flux is unsteady and takes a general separable form is described in Appendix A.

6. The mass of particles

The mass of particles per unit area within the footprint of the droplet is ϕh, and so the mass of particles in the bulk of the droplet as it evaporates, denoted by $M_{drop} = M_{drop}(t)$ (non-dimensionalised by $\hat{\theta}_0\hat{R}_0^3\hat{\phi}_{ref}$), is given by

$$M_{drop} = 2\pi\int_0^1 \phi(r,t)\,h(r,t)\,r\,\mathrm{d}r, \tag{6.1}$$

which can be rewritten as

$$M_{drop} = 2\pi\int_0^{r_0(1,t)} \phi_0(r)\,h(r,0)\,r\,\mathrm{d}r, \tag{6.2}$$

where $r_0(1,t)$ denotes the initial radial position of the particles that are at radial position $r = 1$ (i.e. at the contact line) at time t, which is determined by solving (5.17*a*) with $r = 1$. The initial mass of particles in the droplet is $M_{drop}(0) = M_0$, where

$$M_0 = 2\pi\int_0^1 \phi_0(r)\,h(r,0)\,r\,\mathrm{d}r. \tag{6.3}$$

The mass flux of particles from the bulk of the droplet into the contact line is $\lim_{r\to 1^-} 2\pi r\phi Q$, and so the mass of particles in the ring deposit that can form at the

contact line, denoted by $M_{ring} = M_{ring}(t)$ (also non-dimensionalised by $\hat{\theta}_0 \hat{R}_0^3 \hat{\phi}_{ref}$), is given by

$$M_{ring} = 2\pi \int_0^t \lim_{r \to 1^-} r\, \phi(r, \tilde{t})\, Q(r, \tilde{t})\, \mathrm{d}\tilde{t}, \tag{6.4}$$

which can be rewritten as

$$M_{ring} = 2\pi \int_{r_0(1,t)}^1 \phi_0(r)\, h(r, 0)\, r\, \mathrm{d}r \tag{6.5}$$

(see Deegan *et al.* 2000; Boulogne *et al.* 2017). The initial mass of particles in the ring is, by definition, zero, i.e. $M_{ring}(0) = 0$.

Adding the expressions for M_{drop} and M_{ring}, given by (6.2) and (6.5), respectively, confirms that the total mass of particles is conserved as the droplet evaporates, i.e. that $M_{drop} + M_{ring} \equiv M_0$.

For simplicity, in the remainder of the present work we take the initial concentration of particles in the bulk of the droplet to be spatially uniform, and so, as consequence of our choice of $\hat{\phi}_{ref}$, $\phi_0(r) \equiv 1$. In this case, from (6.3), the initial mass of particles in the droplet is

$$M_0 = 2\pi \int_0^1 h(r, 0)\, r\, \mathrm{d}r = \frac{\pi}{4}. \tag{6.6}$$

7. A one-parameter family of local evaporative fluxes

7.1. *The local evaporative flux*

In the remainder of the present work we analyse the behaviour of the general solutions obtained in §§ 3–6 for a one-parameter family of local evaporative fluxes of the form $J(r) = J_0(1 - r^2)^n$, where, in order to ensure that the total evaporative flux given by (3.10) is finite, the exponent n must satisfy $n > -1$, but is otherwise a free parameter. As mentioned in § 2, this specific form of J was chosen because as n is varied it exhibits qualitatively different behaviours mimicking those that can be obtained by, for example, surrounding the droplet with a bath of fluid or using a mask with one or more holes in it to achieve a desired pattern of evaporation enhancement and/or suppression, as described in § 1. (Note that a similar, but different, variation in the form of J occurs as the contact angle varies over the range $0 < \theta \leqslant \pi$.) In particular, the values $n = -1/2$, $n = 0$ and $n = 1$ correspond to diffusion-limited evaporation into an unbounded atmosphere given by (2.3), spatially uniform evaporation and evaporation that is proportional to $-\partial h/\partial t$, respectively. However, as also mentioned in § 2, the rather general results obtained in the present work do not rely exclusively on this specific motivation for the form of the local evaporative flux.

To facilitate comparison between the results for different values of n, the pre-factor in J was chosen to be $J_0 = J_0(n) = 4(n + 1)/\pi$ so that the total evaporative flux given by (3.10) is equal to its value for diffusion-limited evaporation into an unbounded atmosphere, namely $F = 4$, for all values of n. In particular, this means that the evolution of the droplet given by (3.13), namely

$$\theta = 1 - \frac{16}{\pi} t, \quad V = \frac{\pi}{4} - 4t, \tag{7.1a,b}$$

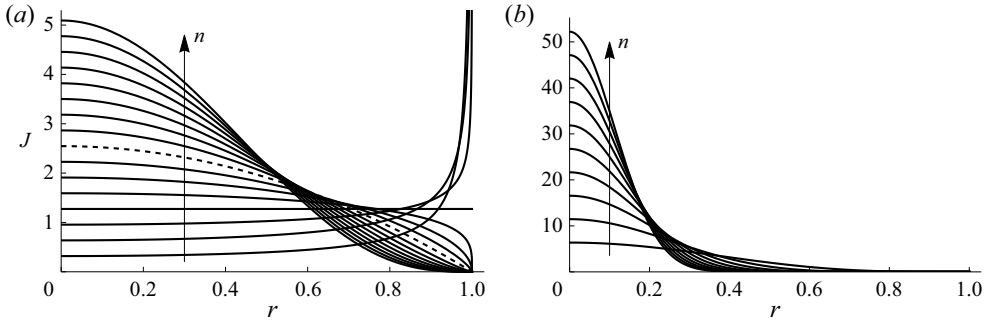

Figure 2. The prescribed local evaporative flux J given by (7.2) plotted as a function of r for (*a*) $n = -3/4, -1/2, \ldots, 3$ and (*b*) $n = 4, 8, \ldots, 40$. In (*a*) the dashed line denotes the curve for $n = 1$. The arrows indicate the direction of increasing n.

and hence the lifetime of the droplet given by (3.14), namely $t_{lifetime} = \pi/16$, are the same for all values of n. Thus in the remainder of the present work we take

$$J(r) = \frac{4(n+1)}{\pi}(1-r^2)^n \quad \text{for } n > -1, \tag{7.2}$$

and, in particular, we will describe the qualitatively different behaviours of the flow within the droplet in § 7.2, the concentration of particles within the droplet in § 7.3 and the masses of the particles in the bulk of the droplet and in the ring deposit in § 7.4 for different values of n.

Figure 2 shows J given by (7.2) plotted as a function of r for a range of values of n. As figure 2 shows, the behaviour of J is qualitatively different for $-1 < n < 0$, $n = 0$, and $n > 0$. For $-1 < n < 0$ (including the special case $n = -1/2$ of diffusion-limited evaporation into an unbounded atmosphere), J is a monotonically increasing function of r which takes its minimum value at the centre of the droplet (i.e. at $r = 0$) and is (integrably) singular at the contact line (i.e. at $r = 1$) according to

$$J \sim \frac{2^{2+n}(n+1)}{\pi}(1-r)^n \quad \text{as } r \to 1^-. \tag{7.3}$$

For $n = 0$ (i.e. spatially uniform evaporation), $J \equiv 4/\pi$, while for $n > 0$ (including the special case $n = 1$ in which J is proportional to $-\partial h/\partial t$), J is a monotonically decreasing function of r which takes its maximum value at the centre of the droplet and approaches zero at the contact line according to (7.3).

7.2. *The flow within the droplet*

Substituting the expression for J given by (7.2) into (3.11) and evaluating the integral gives

$$I = \frac{4(n+1)}{\pi}\int_0^r (1-\tilde{r}^2)^n\,\tilde{r}\,\mathrm{d}\tilde{r} = \frac{2}{\pi}\left[1-(1-r^2)^{n+1}\right], \tag{7.4}$$

and so from (4.11) with (3.8) and (7.4) the radial volume flux Q is given by

$$Q = \frac{2(1-r^2)}{\pi r}\left[(1-r^2)^n - (1-r^2)\right], \tag{7.5}$$

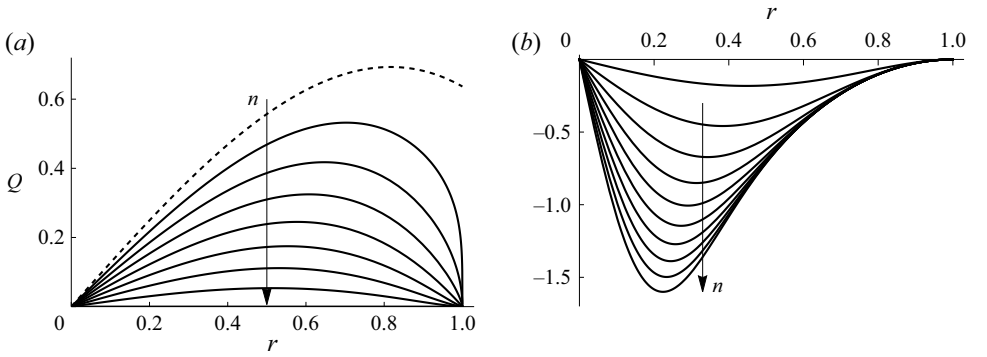

Figure 3. The radial volume flux Q given by (7.5) plotted as a function of r for (*a*) $n = -3/4, -1/2, \ldots, 1$ and (*b*) $n = 2, 4, \ldots, 20$. In (*a*) the dashed line denotes the limiting value of Q as $n \to -1^+$, namely $2r(2 - r^2)/\pi$. The arrows indicate the direction of increasing n.

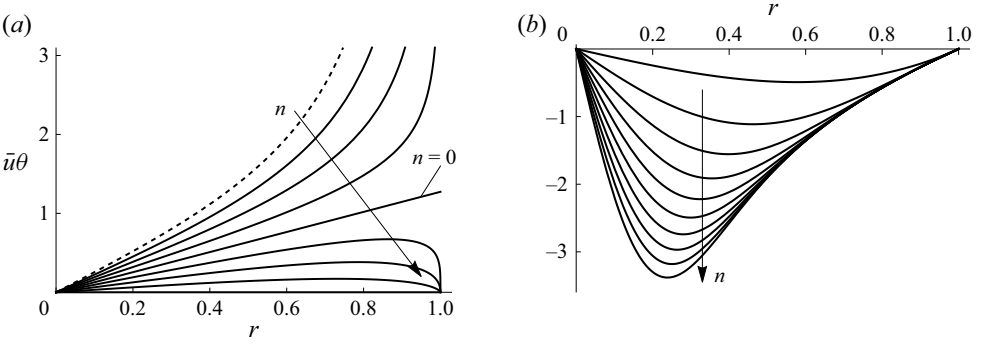

Figure 4. The quantity $\bar{u}\theta$ given by (7.6) plotted as a function of r for (*a*) $n = -3/4, -1/2, \ldots, 1$ and (*b*) $n = 2, 4, \ldots, 20$. In (*a*) the dashed line denotes the limiting value of $\bar{u}\theta$ as $n \to -1^+$, namely $4r(2 - r^2)/(\pi(1 - r^2))$. The arrows indicate the direction of increasing n.

and hence the depth-averaged radial velocity $\bar{u}$ is given by

$$\bar{u} = \frac{Q}{h} = \frac{4}{\pi\theta r}\left[(1 - r^2)^n - (1 - r^2)\right]. \tag{7.6}$$

In the special case $n = 1$ (7.5) and (7.6) give $Q \equiv 0$ and $\bar{u} \equiv 0$, and, as we shall show subsequently, there is no flow within the droplet in this case.

Figures 3 and 4 show Q given by (7.5) and $\bar{u}\theta$ given by (7.6), respectively, for a range of values of n. In particular, figures 3 and 4 show that both Q and $\bar{u}$ are qualitatively different for $-1 < n < 1$ and $n > 1$. Specifically, for $-1 < n < 1$ the average radial velocity is always outwards (i.e. $Q \geqslant 0$ and $\bar{u} \geqslant 0$), whereas for $n > 1$ the average radial velocity is always inwards (i.e. $Q \leqslant 0$ and $\bar{u} \leqslant 0$). However, figures 3 and 4 also show that while Q always approaches zero at $r = 0$ and $r = 1$ and $\bar{u}$ always approaches zero at $r = 0$ according to $\bar{u} \sim 4(1 - n)r/(\pi\theta) \to 0$ as $r \to 0^+$, the behaviour of $\bar{u}$ at $r = 1$ is more complicated. Specifically, for $-1 < n < 0$, $\bar{u}$ is singular according to

$$\bar{u} \sim \frac{2^{2+n}}{\pi\theta}(1 - r)^n \quad \text{as } r \to 1^-, \tag{7.7}$$

for $n = 0$, $\bar{u} = 4/(\pi\theta)$ at $r = 1$, for $0 < n < 1$, $\bar{u}$ approaches zero from above according to (7.7), while for $n \geqslant 1$, $\bar{u}$ approaches zero from below according to

$$\bar{u} \sim -\frac{8}{\pi\theta}(1 - r) \to 0^- \quad \text{as } r \to 1^-. \tag{7.8}$$

Substituting the expression for $\partial p^{(1)}/\partial r$ given by (4.12) into (4.4) and (4.5) yields the solutions for the velocities u and w, namely

$$u = \frac{24z}{\pi\theta^3 r(1 - r^2)^2}\left[(1 - r^2)^n - (1 - r^2)\right]\left[\theta(1 - r^2) - z\right] \tag{7.9}$$

and

$$w = -\frac{8z^2}{\pi\theta^3(1 - r^2)^3}\left[3\theta(1 - n)(1 - r^2)^{n+1} - 2(2 - n)(1 - r^2)^n z + 2(1 - r^2)z\right], \tag{7.10}$$

with (Stokes) streamfunction $\psi = \psi(r, z, t)$ (non-dimensionalised by $\hat{R}_0\hat{U}_{ref}$)

$$\psi = -\frac{4z^2}{\pi\theta^3(1 - r^2)^2}\left[(1 - r^2)^n - (1 - r^2)\right]\left[3\theta(1 - r^2) - 2z\right]. \tag{7.11}$$

In particular, (7.9) shows that the radial velocity u satisfies $u > 0$, $u \equiv 0$ and $u < 0$ everywhere within the droplet when $-1 < n < 1$, $n = 1$ and $n > 1$, respectively, i.e. the radial velocity is always in the same direction as the average radial velocity. However, as (7.10) shows, the behaviour of the vertical velocity w is qualitatively different for $-1 < n \leqslant 1/2$, $1/2 < n < 1$, $n = 1$ and $n > 1$. Specifically, whereas $w < 0$ and $w \equiv 0$ everywhere within the droplet when $-1 < n \leqslant 1/2$ and $n = 1$, respectively, the sign of w is not the same everywhere within the droplet when $1/2 < n < 1$ and when $n > 1$, i.e. there is always both upwards and downwards flow in these cases. Using (7.10) shows that in these cases there is a curve within the droplet on which $w = 0$, denoted by $z = z_{crit}(r, t)$, given by

$$\frac{z_{crit}}{h} = \frac{3(1 - n)}{2 - n - (1 - r^2)^{1-n}} \quad \text{for } r_{crit} \leqslant r \leqslant 1, \tag{7.12}$$

where $r = r_{crit}$ is the solution of $z_{crit}/h = 1$. Specifically, when $1/2 < n < 1$ then $w < 0$ everywhere within the droplet except for $w = 0$ on $z = z_{crit}$ and $w > 0$ for $z_{crit} < z \leqslant h$ and, conversely, when $n > 1$ then $w > 0$ everywhere within the droplet except for $w = 0$ on $z = z_{crit}$ and $w < 0$ for $z_{crit} < z \leqslant h$.

In the special cases $n = -1/2$ and $n = 0$ (7.9) and (7.10) are equivalent to the corresponding expressions given by Boulogne *et al.* (2017). In the special case $n = 1$ (7.9) and (7.10) give $u \equiv 0$ and $w \equiv 0$, i.e. the local mass loss due to evaporation is exactly balanced by the local decrease of the free-surface profile everywhere, and so there is no flow within the droplet.

Note that while J and Q are independent of time t, the quantities $\bar{u}$, u and w all depend on t via their dependence on θ given by (7.1*a*). In particular, $\bar{u}$ is singular in the limit $t \to t^-_{lifetime}$ with $\bar{u} \to +\infty$ for $-1 < n < 1$ and $\bar{u} \to -\infty$ for $n > 1$, where the former behaviour is a generalisation of the rush-hour effect that occurs during the final stages of diffusion-limited evaporation into an effectively unbounded atmosphere mentioned in § 1.

The solution for the first-order pressure $p^{(1)}$ can be obtained by eliminating Q between (4.9) and (7.5) and integrating with respect to r. The resulting expression for $p^{(1)}$ is given by D'Ambrosio (2022), but is rather cumbersome and so is omitted here for brevity.

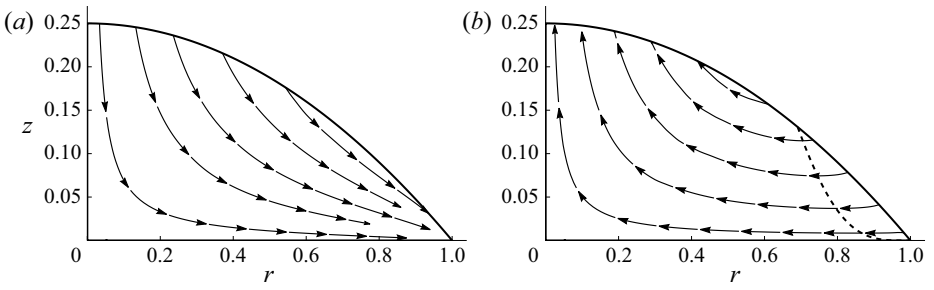

Figure 5. The instantaneous streamlines of the flow within the droplet calculated from (7.9) and (7.10) for (*a*) $n = -1/2$ and (*b*) $n = 4$ at $t = t_{lifetime}/2 = \pi/32$. In (*b*) the dashed line denotes the curve $z = z_{crit}$ on which $w = 0$ given by (7.12).

Figure 5 shows the instantaneous streamlines of the flow within the droplet calculated from (7.9) and (7.10) for (a) $n = -1/2$ (typical of $-1 < n \leqslant 1/2$) and (b) $n = 4$ (typical of $n > 1$) at $t = t_{lifetime}/2 = \pi/32$. (Note that, for brevity, figure 5 does not include a corresponding plot for a value of n in the range $1/2 < n < 1$.) In particular, figure 5(*a*) illustrates that when $n = -1/2$ the flow is outwards and downwards everywhere, while figure 5(*b*) illustrates that when $n = 4$ the flow is inwards and upwards everywhere except for a region of downwards flow for $z_{crit} < z \leqslant h$ when $r_{crit} \simeq 0.6908 < r < 1$, where the curve $z = z_{crit}$ on which $w = 0$ is given by (7.12).

7.3. *The concentration of particles within the droplet*

Substituting the expression for Q given by (7.5) into (5.17*a*) and evaluating the integral gives

$$\theta^{(1-n)/2} = \frac{1-(1-r_0^2)^{1-n}}{1-(1-r^2)^{1-n}}, \tag{7.13}$$

and so, using (7.1*a*), the time for the particles that are at initial radial position r_0 to reach radial position r is given by

$$\frac{t}{t_{lifetime}} = 1 - \left[\frac{1-(1-r_0^2)^{1-n}}{1-(1-r^2)^{1-n}}\right]^{2/(1-n)}. \tag{7.14}$$

In particular, setting $r = 1$ in (7.14), the time for the particles that are at initial radial position r_0 to reach the ring deposit at the contact line, denoted by $t = t_{ring}$, is given by

$$\frac{t_{ring}}{t_{lifetime}} = 1 - \left[1-(1-r_0^2)^{1-n}\right]^{2/(1-n)} \quad \text{for } -1 < n < 1. \tag{7.15}$$

Figure 6 shows $t_{ring}/t_{lifetime}$ given by (7.15) plotted as a function of r_0 for various values of n in the range $-1 < n < 1$. In particular, figure 6 shows that, as expected, $t_{ring}/t_{lifetime}$ decreases monotonically from $t_{ring}/t_{lifetime} = 1$ at $r_0 = 0$ to $t_{ring}/t_{lifetime} = 0$ at $r_0 = 1$, i.e. particles initially close to the contact line are deposited at the contact line before those that are initially further away from it, and all of the particles are eventually transferred from the bulk of the droplet to the ring deposit at the contact line.

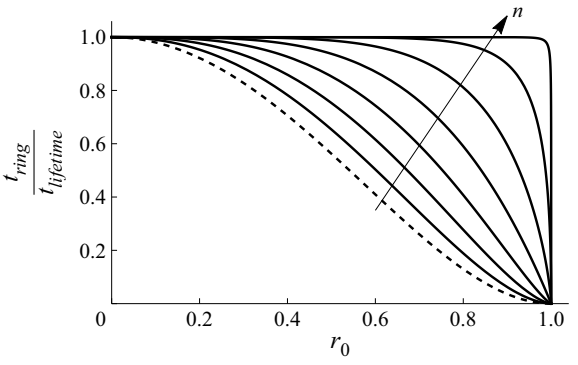

Figure 6. The quantity $t_{ring}/t_{lifetime}$ given by (7.15) as a function of r_0 for $n = -3/4, -1/2, \ldots, 3/4$. The dashed line denotes the limiting value of $t_{ring}/t_{lifetime}$ as $n \to -1^+$, namely $(1 - r_0^2)^2$. The arrow indicates the direction of increasing n.

Substituting the expression for Q given by (7.5) into (5.17b) and using (7.13) gives

$$\phi = \theta^{-(1+n)/2} \left(\frac{1 - r_0^2}{1 - r^2} \right)^{n+1}, \tag{7.16}$$

and eliminating r_0 between (7.13) and (7.16) yields an explicit expression for the concentration of particles within the droplet, namely

$$\phi = \left[\frac{\theta^{(n-1)/2} - 1 + (1 - r^2)^{1-n}}{(1 - r^2)^{1-n}} \right]^{(n+1)/(1-n)}. \tag{7.17}$$

In the special cases $n = -1/2$ and $n = 0$ (7.17) is equivalent to the corresponding expressions given by Zheng (2009).

Figure 7 shows ϕ given by (7.17) plotted as a function of r for a range of values of n at $t = t_{lifetime}/2 = \pi/32$. In particular, figure 7 illustrates that the behaviour of ϕ is qualitatively different for $-1 < n < 1$, $n = 1$ and $n > 1$. Specifically, for $-1 < n < 1$, ϕ is a monotonically increasing function of r which takes its minimum value at $r = 0$ and is singular at the contact line according to $\phi = O((1 - r)^{-(n+1)})$, for $n = 1$, ϕ remains spatially uniform and is given by $\phi = 1/\theta$, while for $n > 1$, ϕ is a monotonically decreasing function of r which takes its maximum value at $r = 0$ and approaches unity from above at the contact line according to $\phi = 1 + O((1 - r)^{n-1})$.

7.4. *The mass of particles*

From (3.5) and (7.17) the mass of particles per unit area is given by

$$\phi h = \frac{\theta(1 - r^2)}{2} \left[\frac{\theta^{(n-1)/2} - 1 + (1 - r^2)^{1-n}}{(1 - r^2)^{1-n}} \right]^{(n+1)/(1-n)}. \tag{7.18}$$

Figure 8 shows ϕh given by (7.18) plotted as a function of r at various times for (a) $n = -1/2$ (typical of $-1 < n < 0$), (b) $n = 0$, (c) $n = 1/2$ (typical of $0 < n < 1$) and (d) $n = 2$ (typical of $n > 1$). Note that, because it is independent of time t, the plot of ϕh in the special case $n = 1$ in which it remains identically equal to its initial value of

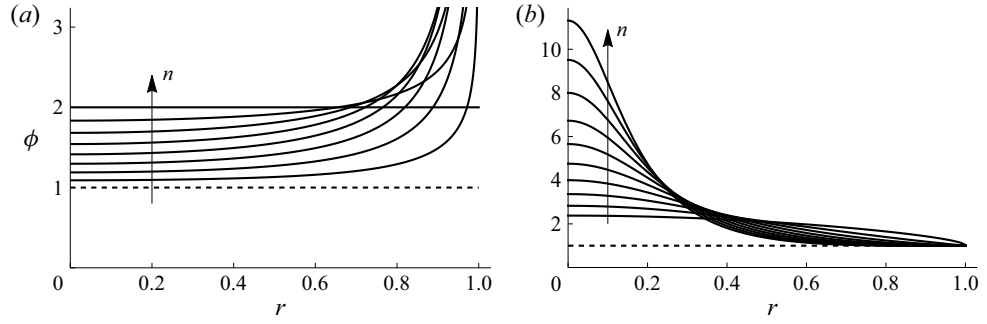

Figure 7. The concentration of particles within the droplet ϕ given by (7.17) plotted as a function of r for (*a*) $n = -3/4, -1/2, \ldots, 1$ and (*b*) $n = 3/2, 2, \ldots, 6$ at $t = t_{lifetime}/2 = \pi/32$. The dashed lines denote the initial concentration of particles, namely $\phi \equiv 1$, which is also the limiting value of ϕ as $n \to -1^+$. The arrows indicate the direction of increasing n.

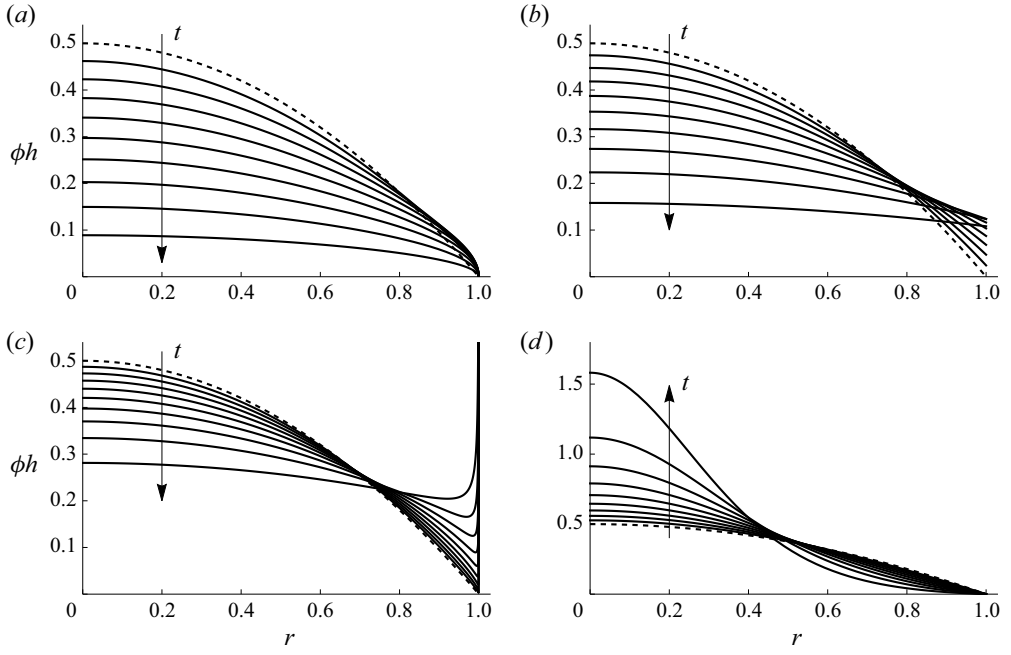

Figure 8. The mass of particles per unit area ϕh given by (7.18) at times $t = (0, 1/10, \ldots, 9/10) \times t_{lifetime}$ for (*a*) $n = -1/2$, (*b*) $n = 0$, (*c*) $n = 1/2$ and (*d*) $n = 2$. The dashed lines denote the initial mass of particles given by $h(r, 0) = (1 - r^2)/2$, and the arrows indicate the direction of increasing t.

$(1 - r^2)/2$ is omitted from figure 8. In particular, figure 8 illustrates that, in addition to the special case $n = 1$, the behaviour of ϕh is qualitatively different for $-1 < n < 0$, $n = 0$, $0 < n < 1$ and $n > 1$. Specifically, figures 8(*a*)–8(*c*) illustrate that for $-1 < n < 1$ (i.e. when the radial flow is outwards) ϕh decreases (relative to its initial value) near the centre of the droplet but increases (again relative to its initial value) near the contact line as the droplet evaporates. However, its behaviour near the contact line depends on the value of n, namely $\phi h = O((1 - r)^{-n}) \to 0^+$ in the limit $r \to 1^-$ when $-1 < n < 0$, $\phi h = \theta^{1/2}(1 - \theta^{1/2})/2 = O(1)$ at $r = 1$ when $n = 0$ and $\phi h = O((1 - r)^{-n}) \to +\infty$ in the limit $r \to 1^-$ when $0 < n < 1$. Since particles are advected towards the contact line by the outwards

radial flow, at first sight, the behaviour of ϕh near the contact line when $-1 < n < 1$ might appear to be surprising. However, this behaviour is explained by the fact that when $-1 < n < 0$ the advection of particles towards the contact line is balanced by the flux into the ring deposit, and hence $\phi h = 0$ at $r = 1$, whereas when $0 \leqslant n < 1$ the advection of particles towards the contact line exceeds the flux into the ring deposit, and hence $\phi h = O(1)$ at $r = 1$ when $n = 0$ and ϕh is unbounded in the limit $r \to 1^-$ when $0 < n < 1$. On the other hand, figure 8(*d*) illustrates that for $n > 1$ (i.e. when the radial flow is inwards) ϕh increases (relative to its initial value) near the centre of the droplet but decreases (again relative to its initial value) near the contact line as the droplet evaporates, and satisfies $\phi h = O(1 - r) \to 0^+$ in the limit $r \to 1^-$.

For $n \geqslant 1$ the radial flow is always inwards (or, in the special case $n = 1$, zero) and so all of the particles remain within the bulk of the droplet as it evaporates. Hence

$$M_{drop} \equiv M_0, \quad M_{ring} \equiv 0 \quad \text{for } n \geqslant 1, \tag{7.19}$$

and no ring deposit forms at the contact line. For $n > 1$ all of the particles are eventually advected to the centre of the droplet, and so the final deposit on the substrate predicted by the model is a deposit of mass M_0 at $r = 0$. Of course, in practice, diffusion in the radial direction, or other weak physical effects not accounted for in the present leading-order model, will smooth this out to create a deposit of non-zero radius near $r = 0$.

In the special case $n = 1$ there is no flow, and so all of the particles are simply deposited onto the substrate at their initial radial position. As a consequence of the paraboloidal shape of the initial free-surface profile of the droplet, and hence of the initial distribution of mass, the distribution of mass in the final deposit on the substrate predicted by the model is also paraboloidal, specifically $(1 - r^2)/2$. This behaviour is consistent with the corresponding experimental results of Deegan *et al.* (2000) for a local evaporative flux that is approximately proportional to the rate of decrease of the height of the droplet discussed in § 1.

For $-1 < n < 1$ the radial flow is always outwards and all of the particles are eventually advected to the contact line. Evaluating M_{drop} and M_{ring} using (6.2) and (6.5), respectively, requires the value of $r_0(1, t)$, i.e. the initial radial position of the particles that are at radial position $r = 1$ at time t, and this is readily obtained from (7.13) to be

$$r_0(1, t) = \left[1 - \left(1 - \theta^{(1-n)/2}\right)^{1/(1-n)}\right]^{1/2} \quad \text{for } -1 < n < 1. \tag{7.20}$$

Substituting the expression for ϕh given by (7.18) into (6.2) and (6.5), and evaluating the integrals using (7.20), yields explicit expressions for the masses of the particles in the bulk of the droplet and in the ring deposit at time t, namely

$$M_{drop} = M_0\left[1 - \left(1 - \theta^{(1-n)/2}\right)^{2/(1-n)}\right] \quad \text{for } 1 < n < 1 \tag{7.21}$$

and

$$M_{ring} = M_0\left(1 - \theta^{(1-n)/2}\right)^{2/(1-n)} \quad \text{for } -1 < n < 1, \tag{7.22}$$

respectively, where the initial mass of particles in the bulk of the droplet is given by (6.6) to be $M_0 = \pi/4$. In the special case $n = -1/2$ (7.22) is equivalent to the corresponding expression first given by Deegan *et al.* (2000), and in the special cases $n = -1/2$ and $n = 0$ it is equivalent to the corresponding expressions given by Boulogne *et al.* (2017). For $-1 < n < 1$ all of the particles are eventually transferred from the bulk of the droplet

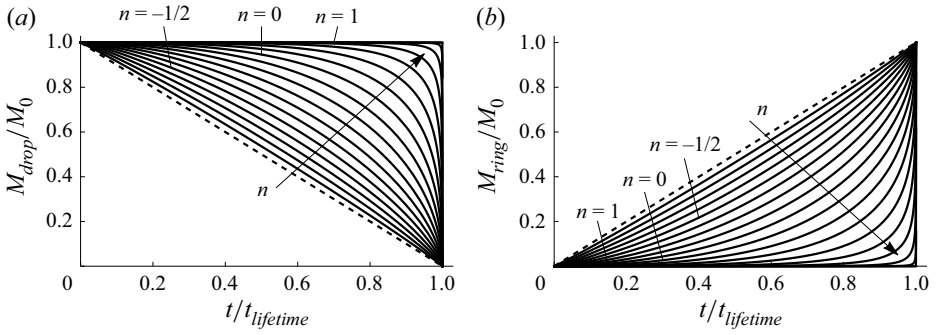

Figure 9. The evolutions of (*a*) M_{drop}/M_0 given by (7.21) and (*b*) M_{ring}/M_0 given by (7.22) as functions of $t/t_{lifetime}$ for $n = -9/10, -4/5, \ldots, 1$. The dashed straight lines denote the limiting values of M_{drop}/M_0 and M_{ring}/M_0 as $n \to -1^+$, namely θ and $1-\theta$, respectively. The arrows indicate the direction of increasing n.

to the ring deposit at the contact line, and so the final deposit on the substrate predicted by the model is a ring deposit with mass M_0 at $r = 1$. This behaviour is consistent with the corresponding experimental results of Deegan *et al.* (2000) and Boulogne *et al.* (2017) for both diffusion-limited evaporation into an effectively unbounded atmosphere and approximately spatially uniform evaporation discussed in § 1. Of course, in practice, weak physical effects not accounted for in the present leading-order model will again smooth this out to create a ring deposit of non-zero width near $r = 1$.

Figure 9 shows the evolutions of M_{drop}/M_0 and M_{ring}/M_0 plotted as functions of $t/t_{lifetime}$ for various values of n in the range $-1 < n \leqslant 1$. In particular, figure 9(*a*) shows that, as expected, for $-1 < n < 1$, M_{drop}/M_0 decreases monotonically from $M_{drop}/M_0 = 1$ at $t/t_{lifetime} = 0$ to $M_{drop}/M_0 = 0$ at $t/t_{lifetime} = 1$, and figure 9(*b*) shows the corresponding behaviour of M_{ring}/M_0, confirming that for $-1 < n < 1$, all of the particles are eventually transferred from the bulk of the droplet to the ring deposit at the contact line. Figure 9 also shows that as n increases from $n = -1$ towards $n = 1$ the flux of particles into the ring deposit becomes increasingly concentrated towards the end of the lifetime of the droplet, i.e. the rush-hour effect becomes more and more dramatic.

7.5. *Behaviour in the singular limit $n \to -1^+$*

In the singular limit $n \to -1^+$ the local evaporative flux takes the form

$$J = \frac{4(n+1)}{\pi(1-r^2)} + \frac{4(n+1)^2}{\pi(1-r^2)}\log(1-r^2) + O\left((n+1)^3\right), \tag{7.23}$$

which approaches zero from above everywhere except in a thin boundary layer of thickness $O(n+1) \ll 1$ near the contact line, and drives an $O(1)$ radially outwards flow given by

$$\bar{u} = \frac{4r(2-r^2)}{\pi\theta(1-r^2)} + O(n+1)\,(>0). \tag{7.24}$$

The concentration of particles in the bulk of the droplet is given by

$$\phi = 1 + \frac{1}{2}\log\left[\frac{\theta^{-1} - 1 + (1-r^2)^2}{(1-r^2)^2}\right](n+1) + O\left((n+1)^2\right) \quad \text{as } n \to -1^+, \tag{7.25}$$

i.e. at leading order ϕ remains equal to its spatially uniform initial value, but at first order it increases non-uniformly. The masses of the particles in the bulk of the droplet and in the

ring deposit are given by

$$M_{drop} = M_0\theta - \frac{M_0}{2}\left[(1-\theta)\log(1-\theta) + \theta\log\theta\right](n+1) + O\left((n+1)^2\right) \to M_0\theta^+ \tag{7.26}$$

and $M_{ring} = M_0 - M_{drop} \to M_0(1-\theta)^-$ as $n \to -1^+$, respectively. Further details of the behaviour in this limit are given D'Ambrosio (2022).

7.6. *Behaviour in the regular limit $n \to 1$*

In the limit $n \to 1$, i.e. approaching the special case $n = 1$ in which J is proportional to $-\partial h/\partial t$, the local evaporative flux takes the form

$$J = \frac{8(1-r^2)}{\pi} + O(n-1), \tag{7.27}$$

which drives a weak $O(n-1) \ll 1$ radial flow given by

$$\bar{u} = \frac{4(1-r^2)\log(1-r^2)}{\pi\theta r}(n-1) + O\left((n-1)^2\right). \tag{7.28}$$

The concentration of particles in the bulk of the droplet is given by

$$\phi = \frac{1}{\theta} + \frac{\log\theta}{2\theta}\left[1 + 2\log(1-r^2)\right](n-1) + O\left((n-1)^2\right) \quad \text{as } n \to 1, \tag{7.29}$$

i.e. at leading order ϕ takes the spatially uniform value $1/\theta$, but at first order it increases for $0 \leqslant r < r_{zero}$ and decreases for $r_{zero} < r \leqslant 1$ when n approaches 1 from above and *vice versa* when n approaches 1 from below, where $r_{zero} = (1-\mathrm{e}^{-1/2})^{1/2} \simeq 0.6273$. The masses of the particles in the bulk of the droplet and in the ring deposit are given by

$$M_{drop} \sim M_0\left[1 - \theta^{1/2}\left(\log\theta^{(n-1)/2}\right)^{2/(1-n)}\right] \to M_0^- \tag{7.30}$$

and $M_{ring} = M_0 - M_{drop} \to 0^+$ as $n \to 1^-$, respectively. Further details of the behaviour in this limit are again given by D'Ambrosio (2022).

7.7. *Behaviour in the limit $n \to +\infty$*

In the limit $n \to +\infty$ the local evaporative flux takes the form

$$J \sim \frac{4n}{\pi}\mathrm{e}^{-nr^2}, \tag{7.31}$$

which, in sharp contrast to its behaviour in the limit $n \to -1^+$ described in § 7.5, approaches zero from above everywhere except in a thin internal layer of thickness $O(1/\sqrt{n}) \ll 1$ near the centre of the droplet, and drives an $O(1)$ radially inwards flow given by

$$\bar{u} \sim -\frac{4}{\pi\theta r}\left(1 - r^2 - \mathrm{e}^{-nr^2}\right) \ (<0). \tag{7.32}$$

The concentration of particles in the bulk of the droplet is given by

$$\phi \sim \left[1 - \left(1 - \theta^{(n-1)/2}\right)\mathrm{e}^{-nr^2}\right]^{-(n+2)/n} \quad \text{as } n \to +\infty, \tag{7.33}$$

i.e. at leading order ϕ remains equal to its spatially uniform initial value everywhere except for in the internal layer, in which it increases non-uniformly. Since $n > 1$, the masses of

the particles in the bulk of the droplet and in the ring deposit are given by (7.19). Further details of the behaviour in this limit are again given by D'Ambrosio (2022).

8. Particle paths when $Pe^* \gg 1$

Thus far we have considered the regime in which diffusion is faster than axial advection but slower than radial advection, corresponding to $\hat{\theta}_0^2 \ll Pe^* \ll 1$. However, as mentioned in § 5, in this section we calculate the paths of the particles in the alternative regime in which diffusion is slower than both axial and radial advection, corresponding to $Pe^* \gg 1$.

In this regime at leading order the particles are simply advected by the flow, and so the particle paths $r = r(t)$ and $z = z(t)$ satisfy

$$\frac{\mathrm{d}r}{\mathrm{d}t} = u, \quad \frac{\mathrm{d}z}{\mathrm{d}t} = w, \tag{8.1a,b}$$

where u and w are given by (4.4) and (4.5), subject to the initial conditions $r(0) = r_0$ $(0 \leqslant r_0 \leqslant 1)$ and $z(0) = z_0$ $(0 \leqslant z_0 \leqslant h(r_0, 0))$. Motivated by experimental observations of the motion of spherical particles (see for example Yunker *et al.* 2011), we make the natural modelling assumption that if a particle reaches the descending free surface of the droplet, then it thereafter stays on (but moves along) the free surface according to

$$\frac{\mathrm{d}r}{\mathrm{d}t} = u\bigg|_{z=h}, \quad \frac{\mathrm{d}z}{\mathrm{d}t} = w\bigg|_{z=h} - J = \frac{\partial h}{\partial t} + u\bigg|_{z=h}\frac{\partial h}{\partial r} \quad \text{on } z = h, \tag{8.2}$$

without affecting the shape of the droplet or the flow within it. We refer to this as 'free-surface capture' and denote the time at which free-surface capture occurs by $t = t_{capture}$ $(0 \leqslant t_{capture} \leqslant t_{lifetime})$.

For the one-parameter family of local evaporative fluxes given by (7.2), the particle paths are determined by solving (8.1) and (8.2) with u and w given by (7.9) and (7.10), respectively.

In the special case $n = 1$ there is no flow (i.e. $u \equiv 0$ and $w \equiv 0$), and so all of the particles remain at their initial positions as the droplet evaporates until the particle initially at $r = r_0$ and $z = z_0$ is captured by the free surface at time $t = t_{capture}$ given by

$$\frac{t_{capture}}{t_{lifetime}} = \frac{1 - r_0^2 - 2z_0}{1 - r_0^2}. \tag{8.3}$$

Thereafter (i.e. for $t_{capture} < t < t_{lifetime}$) the particle moves vertically downwards on the descending free surface, and is eventually deposited onto the substrate at $r = r_0$ and $z = 0$ at $t = t_{lifetime}$. Hence, as discussed in § 7.3, as a consequence of the paraboloidal shape of the initial free-surface profile of the droplet, the distribution of mass in the final deposit on the substrate predicted by the model is also paraboloidal, specifically $(1 - r^2)/2$.

In the general case $-1 < n < 1$ and $n > 1$ the particle paths were determined by solving (8.1) and (8.2) numerically using the NDSolve function in Mathematica 12.2 (Wolfram Research, Inc. 2021).

Figure 10 shows the paths taken by the particle that starts at the initial position $r_0 = 1/2$ and $z_0 = 1/4$ for a range of values of n. In particular, figure 10 shows that, as a consequence of the behaviour of the flow described in § 7.2, before it is captured by the free surface, this particle moves downwards and outwards when $-1 < n < 1$, remains stationary when $n = 1$, moves upwards and inwards when $1 < n < n_{crit} \simeq 14.47$, and initially moves downwards and inwards and then upwards and inwards when $n > n_{crit}$, where $n = n_{crit}$

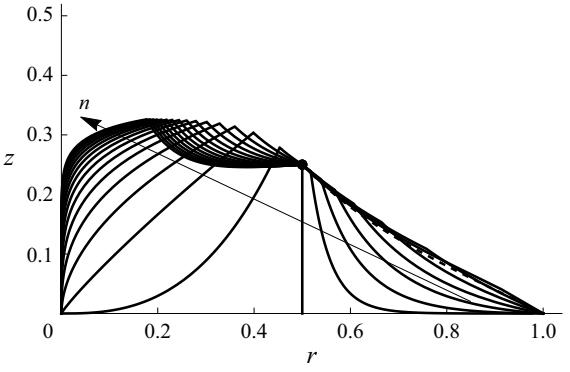

Figure 10. The paths taken by the particle that starts at the initial position $r_0 = 1/2$ and $z_0 = 1/4$ for $n = -3/4, -1/2, \ldots, 1, 2, 4, \ldots, 30$. The (barely discernible) dashed line denotes the limiting particle path as $n \to -1^+$, and the arrow indicates the direction of increasing n.

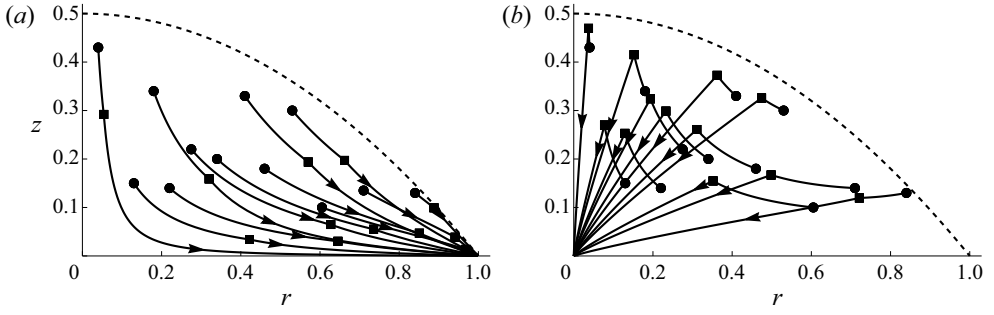

Figure 11. The paths of twelve representative particles for (*a*) $n = -1/2$ and (*b*) $n = 4$. The dots and the squares denote the initial position and the position of free-surface capture, respectively, of each particle. The dashed lines denote the initial free-surface profile given by $h(r, 0) = (1 - r^2)/2$.

is the solution of $z_{crit}(r_0, 0) = z_0$. Figure 10 also shows that after it is captured by the descending free surface, this particle continues to move downwards and outwards when $-1 < n < 1$, moves vertically downwards when $n = 1$, and moves downwards and inwards when $n > 1$. Figure 10 also confirms that the final position of this particle on the substrate is in the ring deposit at $r = 1$ when $-1 < n < 1$, at $r = r_0$ when $n = 1$, and at the centre of the droplet at $r = 0$ when $n > 1$.

Figure 11 shows the paths of twelve representative particles for (*a*) $n = -1/2$ (typical of $-1 < n \leqslant 1/2$) and (*b*) $n = 4$ (typical of $n > 1$). (Note that, for brevity, figure 11 does not include a corresponding plot for a value of n in the range $1/2 < n < 1$.) The dots and the squares denote the initial position and the position of free-surface capture, respectively, of each particle. Figure 11 illustrates that all of the particles are captured by the free surface before eventually being deposited onto the substrate. This behaviour is consistent with the numerical results of Kang *et al.* (2016) for diffusion-limited evaporation of a non-thin droplet. Note that, unlike all of the particles shown in figure 11(*a*) and the other eleven particles shown in figure 11(*b*), which move upwards before being captured by the descending free surface, the rightmost particle shown in figure 11(*b*) (i.e. the one with initial position $r_0 = 0.84$ and $z_0 = 0.13$ satisfying $z_{crit}(r_0, 0) < z_0 < h(r_0, 0)$) moves downwards before being captured.

9. Conclusions

Motivated by the continuing interest in controlling the deposition from an evaporating droplet, in the present work we analysed the effect of the spatial variation of the local evaporative flux on the deposition from a pinned particle-laden sessile droplet. Specifically, in §§ 2–6 we formulated and solved a mathematical model for the evolution of a thin sessile droplet with a general prescribed steady local evaporative flux $J(r)$, the flow within the droplet, the concentration of particles within the droplet and the masses of the particles in the bulk of the droplet and in the ring deposit that can form at the contact line. Then in §§ 7 and 8 we analysed the behaviour of the general solutions obtained in §§ 3–6 for the one-parameter family of local evaporative fluxes $J(r)$ given by (7.2) with the free parameter $n\,(> -1)$ that exhibits qualitatively different behaviours mimicking those that can be obtained by, for example, surrounding the droplet with a bath of fluid or using a mask with one or more holes in it to achieve a desired pattern of evaporation enhancement and/or suppression, as described in § 1. Specifically, for $-1 < n < 0$ (including the special case $n = -1/2$ of diffusion-limited evaporation into an unbounded atmosphere), J is (integrably) singular at the contact line and smallest at the centre of the droplet, for $n = 0$, J is spatially uniform, while for $n > 0$ (including the special case $n = 1$ in which J is proportional to $-\partial h/\partial t$), J is largest at the centre of the droplet and zero at the contact line. In particular, we obtained explicit expressions for the concentration of particles within the bulk of the droplet ϕ given by (7.17) and the masses of the particles in the bulk of the droplet and in the ring deposit M_{drop} and M_{ring} given by (7.21) and (7.22), respectively, which generalise the previous results in the special cases $n = -1/2$, $n = 0$ and $n = 1$ described in § 1. We showed that, while the behaviour of the vertical velocity w given by (7.10) is qualitatively different for $-1 < n \leqslant 1/2$, $1/2 < n < 1$, $n = 1$ and $n > 1$, the radial velocity u given by (7.9) is always outwards towards the contact line when $-1 < n < 1$, but inwards towards the centre of the droplet when $n > 1$. In the former case all of the particles are eventually advected to the contact line, and so the final deposit is a ring deposit at $r = 1$, whereas in the latter case all of the particles are eventually advected to the centre of the droplet, and so the final deposit is at $r = 0$. In the special case $n = 1$ in which J is proportional to $-\partial h/\partial t$ the local mass loss due to evaporation is exactly balanced by the local decrease of the free-surface profile everywhere, and so there is no flow within the droplet and the final deposit has a paraboloidal profile. In particular, the present work demonstrates that, contrary to what is sometimes erroneously implicitly implied or explicitly claimed, a singular (or even a non-zero) evaporative flux at the contact line is not an essential requirement for the formation of a ring deposit. Indeed, not only a spatially uniform evaporative flux, but also evaporative fluxes with $0 < n < 1$ that are largest at the centre of the droplet and zero at the contact line, lead to the formation of a ring deposit. We also described a generalisation of the well-known rush-hour effect, and found that it becomes more and more dramatic as n increases from $n = -1$ towards $n = 1$. In addition, we calculated the paths of the particles when $Pe^* \gg 1$, and showed that in this regime all of the particles are captured by the descending free surface before eventually being deposited onto the substrate. In particular, the behaviour for $-1 < n < 1$ is consistent with the numerical results of Kang *et al.* (2016) for diffusion-limited evaporation of a non-thin droplet described in § 8.

In Appendix A we showed how the present analysis can be generalised to the situation in which the local evaporative flux is unsteady and takes a general separable form. However, there are many other promising directions for future work. In particular, as well as including additional physical effects, such as when the presence of the particles affects the flow within the droplet (see for example Kaplan & Mahadevan 2015) and/or

particle adsorption and coagulation (see for example Zigelman & Manor 2018*a*), it would be interesting to investigate the effect of the spatial variation of the local evaporative flux in more complicated geometries such as, for example, a non-axisymmetric droplet (see for example Sáenz *et al.* 2017; Wray & Moore 2023), a droplet in a well (see for example Vlasko-Vlasov *et al.* 2020; D'Ambrosio *et al.* 2021) and multiple interacting droplets (see for example Wray *et al.* 2020, 2021).

Funding. H.-M.D'A. acknowledges financial support from the United Kingdom Engineering and Physical Sciences Research Council (EPSRC) via EPSRC Doctoral Training Partnership grant EP/R512205/1 and Strategic Projects CSV-NHFP grant EP/W522521/1 and Merck Chemicals Ltd.

Declaration of interests. The authors report no conflict of interest.

Author ORCIDs.
Hannah-May D'Ambrosio https://orcid.org/0000-0001-5457-5916;
Stephen K. Wilson https://orcid.org/0000-0001-7841-9643;
Alexander W. Wray https://orcid.org/0000-0002-3219-8272.

Appendix A. Unsteady local evaporative flux in separable form

In this appendix we show how the present analysis can be generalised to the situation in which the local evaporative flux is unsteady and takes the general separable form $J = J(r, t) = f(r)g(t)$, where f and g are prescribed functions of r and t, respectively.

In this situation, the total evaporative flux is given by

$$F = 2\pi \int_0^1 J(\tilde{r}, t)\, \tilde{r}\, \mathrm{d}\tilde{r} = 2\pi I(1) g(t), \tag{A1}$$

in which, instead of (3.11), $I = I(r)$ is now defined by

$$I = \int_0^r f(\tilde{r})\, \tilde{r}\, \mathrm{d}r, \tag{A2}$$

and so the droplet evolves according to

$$\theta = 1 - \frac{I(1)G(t)}{H(1)}, \quad V = \frac{\pi}{4}\left(1 - \frac{I(1)G(t)}{H(1)}\right), \tag{A3a,b}$$

in which $G = G(t)$, defined by

$$G = \int_0^t g(\tilde{t})\, \mathrm{d}\tilde{t}, \tag{A4}$$

is the incomplete temporal integral of g.

The local radial volume flux $Q = Q(r, t)$ is given by $Q = q(r)g(t)$, where $q = q(r)$ coincides exactly with the expression for Q when J is independent of t given by (4.11). The characteristic equations (5.12) can therefore be expressed as

$$\frac{\mathrm{d}r}{\mathrm{d}\theta} = \frac{\mathrm{d}r/\mathrm{d}t}{\mathrm{d}\theta/\mathrm{d}t} = -\frac{H(1)q(r)}{\theta I(1)\eta(r)}, \quad \frac{\mathrm{d}\phi}{\mathrm{d}r} = \frac{\mathrm{d}\phi/\mathrm{d}t}{\mathrm{d}r/\mathrm{d}t} = \frac{f(r)\phi}{q(r)}. \tag{A5a,b}$$

A notable feature of these equations is that they do not involve g, and so they coincide exactly with the corresponding equations when J is independent of t given by (5.13) if $J(r)$ is replaced by $f(r)$ and $Q(r)$ is replaced by $q(r)$. In particular, this means that the solution of (A5) can readily be obtained from the solution of (5.13) given by (5.17), and

the unsteadiness of J enters the solution for r_0, and hence the solution for ϕ, only via θ given by (A3*a*).

Once ϕ has been determined, the masses of the particles in the bulk of the droplet and in ring deposit can be calculated from (6.2) and (6.5), respectively.

References

Al-Milaji, K.N. & Zhao, H. 2019 New perspective of mitigating the coffee-ring effect: interfacial assembly. *J. Phys. Chem.* C **123** (19), 12029–12041.

Anyfantakis, M. & Baigl, D. 2015 Manipulating the coffee-ring effect: interactions at work. *ChemPhysChem* **16** (13), 2726–2734.

Anyfantakis, M., Baigl, D. & Binks, B.P. 2017 Evaporation of drops containing silica nanoparticles of varying hydrophobicities: exploiting particle–particle interactions for additive-free tunable deposit morphology. *Langmuir* **33** (20), 5025–5036.

Anyfantakis, M., Geng, Z., Morel, M., Rudiuk, S. & Baigl, D. 2015 Modulation of the coffee-ring effect in particle/surfactant mixtures: the importance of particle–interface interactions. *Langmuir* **31** (14), 4113–4120.

Askounis, A., Sefiane, K., Koutsos, V. & Shanahan, M.E.R. 2013 Structural transitions in a ring stain created at the contact line of evaporating nanosuspension sessile drops. *Phys. Rev.* E **81** (1), 012301.

Askounis, A., Sefiane, K., Koutsos, V. & Shanahan, M.E.R. 2014 The effect of evaporation kinetics on nanoparticle structuring within contact line deposits of volatile drops. *Colloids Surf.* A **441**, 855–866.

Barash, L.Yu., Bigioni, T.P., Vinokur, V.M. & Shchur, L.N. 2009 Evaporation and fluid dynamics of a sessile drop of capillary size. *Phys. Rev.* E **79** (4), 046301.

Berteloot, G., Hoang, A., Daerr, A., Kavehpour, H.P., Lequeux, F. & Limat, L. 2012 Evaporation of a sessile droplet: inside the coffee stain. *J. Colloid Interface Sci.* **370** (1), 155–161.

Bhardwaj, R., Fang, X., Somasundaran, P. & Attinger, D. 2010 Self-assembly of colloidal particles from evaporating droplets: role of DLVO interactions and proposition of a phase diagram. *Langmuir* **26** (11), 7833–7842.

Bodiguel, H. & Leng, J. 2010 Imaging the drying of a colloidal suspension. *Soft Matt.* **6** (21), 5451–5460.

Bou Zeid, W. & Brutin, D. 2013 Influence of relative humidity on spreading, pattern formation and adhesion of a drying drop of whole blood. *Colloids Surf.* A **430**, 1–7.

Boulogne, F., Ingremeau, F. & Stone, H.A. 2017 Coffee-stain growth dynamics on dry and wet surfaces. *J. Phys.: Condens. Matter* **29** (7), 074001.

Brutin, D. (Ed.) 2015 *Droplet Wetting and Evaporation: From Pure to Complex Fluids*. Academic.

Brutin, D. & Sefiane, K. (Eds) 2022 *Drying of Complex Fluid Drops: Fundamentals and Applications*. Soft Matter Series No. 14. Royal Society of Chemistry.

Brutin, D. & Starov, V. 2018 Recent advances in droplet wetting and evaporation. *Chem. Soc. Rev.* **47** (2), 558–585.

Cazabat, A.-M. & Guéna, G. 2010 Evaporation of macroscopic sessile droplets. *Soft Matt.* **6** (12), 2591–2612.

Chhasatia, V.H., Joshi, A.S. & Sun, Y. 2010 Effect of relative humidity on contact angle and particle deposition morphology of an evaporating colloidal drop. *Appl. Phys. Lett.* **97** (23), 231909.

Crivoi, A. & Duan, F. 2013 Elimination of the coffee-ring effect by promoting particle adsorption and long-range interaction. *Langmuir* **29** (39), 12067–12074.

Crivoi, A., Zhong, X. & Duan, F. 2015 Crossover from the coffee-ring effect to the uniform deposit caused by irreversible cluster-cluster aggregation. *Phys. Rev.* E **92** (3), 032302.

D'Ambrosio, H.-M. 2022 On the evolution of and the deposition from an evaporating sessile droplet. PhD thesis, University of Strathclyde.

D'Ambrosio, H.-M., Colosimo, T., Duffy, B.R., Wilson, S.K., Yang, L., Bain, C.D. & Walker, D.E. 2021 Evaporation of a thin droplet in a shallow well: theory and experiment. *J. Fluid Mech.* **927**, A43.

Deegan, R.D. 2000 Pattern formation in drying drops. *Phys. Rev.* E **61** (1), 475–485.

Deegan, R.D., Bakajin, O., Dupont, T.F., Huber, G., Nagel, S.R. & Witten, T.A. 1997 Capillary flow as the cause of ring stains from dried liquid drops. *Nature* **389** (6653), 827–829.

Deegan, R.D., Bakajin, O., Dupont, T.F., Huber, G., Nagel, S.R. & Witten, T.A. 2000 Contact line deposits in an evaporating drop. *Phys. Rev.* E **62** (1), 756–765.

Dugas, V., Broutin, J. & Souteyrand, E. 2005 Droplet evaporation study applied to DNA chip manufacturing. *Langmuir* **21** (20), 9130–9136.

ERAL, H.B., AUGUSTINE, D.M., DUITS, M.H.G. & MUGELE, F. 2011 Suppressing the coffee stain effect: how to control colloidal self-assembly in evaporating drops using electrowetting. *Soft Matt.* **7** (10), 4954–4958.

ERBIL, H.Y. 2012 Evaporation of pure liquid sessile and spherical suspended drops: a review. *Adv. Colloid Interface Sci.* **170** (1–2), 67–86.

FISCHER, B.J. 2002 Particle convection in an evaporating colloidal droplet. *Langmuir* **18** (1), 60–67.

GARCIA-CORDERO, J.L. & FAN, Z.H. 2017 Sessile droplets for chemical and biological assays. *Lab on a Chip* **17** (13), 2150–2166.

GELDERBLOM, H., DIDDENS, C. & MARIN, A. 2022 Evaporation-driven liquid flow in sessile droplets. *Soft Matt.* **18** (45), 8535–8553.

GEORGIADIS, A., MUHAMAD, F.N., UTGENANNT, A. & KEDDIE, J.L. 2013 Aesthetically textured, hard latex coatings by fast IR-assisted evaporative lithography. *Prog. Org. Coat.* **76** (12), 1786–1791.

GIORGIUTTI-DAUPHINÉ, F. & PAUCHARD, L. 2018 Drying drops. *Eur. Phys. J.* E **41** (3), 32.

HAMAMOTO, Y., CHRISTY, J.R.E. & SEFIANE, K. 2011 Order-of-magnitude increase in flow velocity driven by mass conservation during the evaporation of sessile drops. *Phys. Rev.* E **83** (5), 051602.

HARRIS, D.J., CONRAD, J.C. & LEWIS, J.A. 2009 Evaporative lithographic patterning of binary colloidal films. *Phil. Trans. R. Soc. Lond.* A **367** (1909), 5157–5165.

HARRIS, D.J., HU, H., CONRAD, J.C. & LEWIS, J.A. 2007 Patterning colloidal films via evaporative lithography. *Phys. Rev. Lett.* **98** (14), 148301.

HARRIS, D.J. & LEWIS, J.A. 2008 Marangoni effects on evaporative lithographic patterning of colloidal films. *Langmuir* **24** (8), 3681–3685.

HONG, S.W., XU, J. & LIN, Z. 2006 Template-assisted formation of gradient concentric gold rings. *Nano Lett.* **6** (12), 2949–2954.

HU, H. & LARSON, R.G. 2005 Analysis of the microfluid flow in an evaporating sessile droplet. *Langmuir* **21** (9), 3963–3971.

HU, H. & LARSON, R.G. 2006 Marangoni effect reverses coffee-ring depositions. *J. Phys. Chem.* B **110** (14), 7090–7094.

KAJIYA, T., KANEKO, D. & DOI, M. 2008 Dynamical visualization of "coffee stain phenomenon" in droplets of polymer solution via fluorescent microscopy. *Langmuir* **24** (21), 12369–12374.

KANG, S.J., VANDADI, V., FELSKE, J.D. & MASOUD, H. 2016 Alternative mechanism for coffee-ring deposition based on active role of free surface. *Phys. Rev.* E **94** (6), 063104.

KAPLAN, C.N. & MAHADEVAN, L. 2015 Evaporation-driven ring and film deposition from colloidal droplets. *J. Fluid Mech.* **781**, R2.

KIM, H., BOULOGNE, F., UM, E., JACOBI, I., BUTTON, E. & STONE, H.A. 2016 Controlled uniform coating from the interplay of Marangoni flows and surface-adsorbed macromolecules. *Phys. Rev. Lett.* **116** (12), 124501.

KOLEGOV, K.S. & BARASH, L.YU. 2020 Applying droplets and films in evaporative lithography. *Adv. Colloid Interface Sci.* **285**, 102271.

KOVALCHUK, N.M., TRYBALA, A. & STAROV, V.M. 2014 Evaporation of sessile droplets. *Curr. Opin. Colloid Interface Sci.* **19** (4), 336–342.

KUANG, M., WANG, L. & SONG, Y. 2014 Controllable printing droplets for high-resolution patterns. *Adv. Mater.* **26** (40), 6950–6958.

KUDINA, O., ERAL, B. & MUGELE, F. 2016 e-MALDI: an electrowetting-enhanced drop drying method for MALDI mass spectrometry. *Anal. Chem.* **88** (9), 4669–4675.

LARSON, R.G. 2014 Transport and deposition patterns in drying sessile droplets. *AIChE J.* **60** (5), 1538–1571.

LAYANI, M., GRUCHKO, M., MILO, O., BALBERG, I., AZULAY, D. & MAGDASSI, S. 2009 Transparent conductive coatings by printing coffee ring arrays obtained at room temperature. *ACS Nano* **3** (11), 3537–3542.

LI, Y., DIDDENS, C., SEGERS, T., WIJSHOFF, H., VERSLUIS, M. & LOHSE, D. 2020 Evaporating droplets on oil-wetted surfaces: suppression of the coffee-stain effect. *Proc. Natl Acad. Sci. USA* **117** (29), 16756–16763.

LOHSE, D. & ZHANG, X. 2015 Surface nanobubbles and nanodroplets. *Rev. Mod. Phys.* **87** (3), 981–1035.

MALINOWSKI, R., VOLPE, G., PARKIN, I.P. & VOLPE, G. 2018 Dynamic control of particle deposition in evaporating droplets by an external point source of vapor. *J. Phys. Chem. Lett.* **9** (3), 659–664.

MAMPALLIL, D. & ERAL, H.B. 2018 A review on suppression and utilization of the coffee-ring effect. *Adv. Colloid Interface Sci.* **252**, 38–54.

MAN, X. & DOI, M. 2016 Ring to mountain transition in deposition pattern of drying droplets. *Phys. Rev. Lett.* **116** (6), 066101.

MARÍN, Á.G., GELDERBLOM, H., LOHSE, D. & SNOEIJER, J.H. 2011*a* Order-to-disorder transition in ring-shaped colloidal stains. *Phys. Rev. Lett.* **107** (8), 085502.

MARÍN, Á.G., GELDERBLOM, H., LOHSE, D. & SNOEIJER, J.H. 2011*b* Rush-hour in evaporating coffee drops. *Phys. Fluids* **23** (9), 091111.

MASOUD, H. & FELSKE, J.D. 2009 Analytical solution for Stokes flow inside an evaporating sessile drop: spherical and cylindrical cap shapes. *Phys. Fluids* **21** (4), 042102.

MOORE, M.R., VELLA, D. & OLIVER, J.M. 2021 The nascent coffee ring: how solute diffusion counters advection. *J. Fluid Mech.* **920**, A54.

PARK, J. & MOON, J. 2006 Control of colloidal particle deposit patterns within picoliter droplets ejected by ink-jet printing. *Langmuir* **22** (8), 3506–3513.

PARSA, M., HARMAND, S. & SEFIANE, K. 2018 Mechanisms of pattern formation from dried sessile drops. *Adv. Colloid Interface Sci.* **254**, 22–47.

PARSA, M., HARMAND, S., SEFIANE, K., BIGERELLE, M. & DELTOMBE, R. 2015 Effect of substrate temperature on pattern formation of nanoparticles from volatile drops. *Langmuir* **31** (11), 3354–3367.

PATIL, N.D., BANGE, P.G., BHARDWAJ, R. & SHARMA, A. 2016 Effects of substrate heating and wettability on evaporation dynamics and deposition patterns for a sessile water droplet containing colloidal particles. *Langmuir* **32** (45), 11958–11972.

PICKNETT, P.G. & BEXON, R. 1977 The evaporation of sessile or pendant drops in still air. *J. Colloid Interface Sci.* **61** (2), 336–350.

POPOV, YU.O. 2005 Evaporative deposition patterns: spatial dimensions of the deposit. *Phys. Rev.* E **71** (3), 036313.

RISTENPART, W.D., KIM, P.G., DOMINGUES, C., WAN, J. & STONE, H.A. 2007 Influence of substrate conductivity on circulation reversal in evaporating drops. *Phys. Rev. Lett.* **99** (23), 234502.

ROUTH, A.F. 2013 Drying of thin colloidal films. *Rep. Prog. Phys.* **76** (4), 046603.

ROUTH, A.F. & RUSSEL, W.B. 1998 Horizontal drying fronts during solvent evaporation from latex films. *AIChE J.* **44** (9), 2088–2098.

SÁENZ, P.J., WRAY, A.W., CHE, Z., MATAR, O.K., VALLURI, P., KIM, J. & SEFIANE, K. 2017 Dynamics and universal scaling law in geometrically-controlled sessile drop evaporation. *Nat. Commun.* **8**, 14783.

SEFIANE, K. 2014 Patterns from drying drops. *Adv. Colloid Interface Sci.* **206**, 372–381.

SHAO, X., DUAN, F., HOU, Y. & ZHONG, X. 2020 Role of surfactant in controlling the deposition pattern of a particle-laden droplet: fundamentals and strategies. *Adv. Colloid Interface Sci.* **275**, 102049.

STAUBER, J.M., WILSON, S.K., DUFFY, B.R. & SEFIANE, K. 2014 On the lifetimes of evaporating droplets. *J. Fluid Mech.* **744**, R2.

TALBOT, E., BAIN, C., DE DIER, R., SEMPELS, W. & VERMANT, J. 2016 Droplets drying on surfaces. In *Fundamentals of Inkjet Printing* (ed. S.D. Hoath), chap. 10, pp. 251–279. Wiley–VCH.

TARASEVICH, YU.YU., VODOLAZSKAYA, I.V. & ISAKOVA, O.P. 2011 Desiccating colloidal sessile drop: dynamics of shape and concentration. *Colloid Polym. Sci.* **289** (9), 1015–1023.

TARASEVICH, YU.YU., VODOLAZSKAYA, I.V. & SAKHAROVA, L.V. 2016 Mathematical modeling of pattern formation caused by drying of colloidal film under a mask. *Eur. Phys. J.* E **39** (2), 26.

THAMPI, S.P. & BASAVARAJ, M.G. 2023 Drying drops of colloidal dispersions. *Annu. Rev. Chem. Biomol. Engng* **14**, 53–83.

TRANTUM, J.R., WRIGHT, D.W. & HASELTON, F.R. 2012 Biomarker-mediated disruption of coffee-ring formation as a low resource diagnostic indicator. *Langmuir* **28** (4), 2187–2193.

TREDENICK, E.C., FORSTER, W.A., PETHIYAGODA, R., VAN LEEUWEN, R.M. & MCCUE, S.W. 2021 Evaporating droplets on inclined plant leaves and synthetic surfaces: experiments and mathematical models. *J. Colloid Interface Sci.* **592**, 329–341.

VLASKO-VLASOV, V.K., SULWER, M., SHEVCHENKO, E.V., PARKER, J. & KWOK, W.K. 2020 Ring patterns generated by an expanding colloidal meniscus. *Phys. Rev.* E **102** (5), 052608.

VODOLAZSKAYA, I.V. & TARASEVICH, YU.YU. 2011 The model of drying sessile drop of colloidal solution. *Mod. Phys. Lett.* B **25** (15), 1303–1310.

VODOLAZSKAYA, I.V. & TARASEVICH, YU.YU. 2017 Modeling of mass transfer in a film of solution evaporating under the mask with holes. *Eur. Phys. J.* E **40** (10), 83.

WILSON, S.K. & D'AMBROSIO, H.-M. 2023 Evaporation of sessile droplets. *Annu. Rev. Fluid Mech.* **55**, 481–509.

WILSON, S.K. & DUFFY, B.R. 2022 Mathematical models for the evaporation of sessile droplets. In *Drying of Complex Fluid Drops: Fundamentals and Applications* (ed. D. Brutin & K. Sefiane), Soft Matter Series No. 14, chap. 4, pp. 47–67. Royal Society of Chemistry.

WOLFRAM RESEARCH, INC. 2021 Mathematica, Version 12.2. Champaign, IL.

WRAY, A.W., DUFFY, B.R. & WILSON, S.K. 2020 Competitive evaporation of multiple sessile droplets. *J. Fluid Mech.* **884**, A45.

WRAY, A.W. & MOORE, M.R. 2023 Evaporation of non-circular droplets. *J. Fluid Mech.* **961**, A11.

WRAY, A.W., PAPAGEORGIOU, D.T., CRASTER, R.V., SEFIANE, K. & MATAR, O.K. 2014 Electrostatic suppression of the "coffee stain effect". *Langmuir* **30** (20), 5849–5858.

WRAY, A.W., WRAY, P.S., DUFFY, B.R. & WILSON, S.K. 2021 Contact-line deposits from multiple evaporating droplets. *Phys. Rev. Fluids* **6** (7), 073604.

YANG, Q., GAO, Y., HE, F. & HAO, P. 2021 Patterning in colloidal droplets by forced airflow. *J. Appl. Phys.* **129** (2), 024701.

YANG, X., JIANG, Z., LYU, P., DING, Z. & MAN, X. 2021 Deposition pattern of drying droplets. *Commun. Theor. Phys.* **73** (4), 047601.

YUNKER, P.J., STILL, T., LOHR, M.A. & YODH, A.G. 2011 Suppression of the coffee-ring effect by shape-dependent capillary interactions. *Nature* **476** (7360), 308–311.

ZANG, D., TARAFDAR, S., TARASEVICH, YU.YU., CHOUDHURY, M.D. & DUTTA, T. 2019 Evaporation of a droplet: from physics to applications. *Phys. Rep.* **804**, 1–56.

ZHENG, R. 2009 A study of the evaporative deposition process: pipes and truncated transport dynamics. *Eur. Phys. J.* E **29** (2), 205–218.

ZHONG, X., CRIVOI, A. & DUAN, F. 2015 Sessile nanofluid droplet drying. *Adv. Colloid Interface Sci.* **217**, 13–30.

ZIGELMAN, A. & MANOR, O. 2018*a* The deposition of colloidal particles from a sessile drop of a volatile suspension subject to particle adsorption and coagulation. *J. Colloid Interface Sci.* **509**, 195–208.

ZIGELMAN, A. & MANOR, O. 2018*b* Simulations of the dynamic deposition of colloidal particles from a volatile sessile drop. *J. Colloid Interface Sci.* **525**, 282–290.